EFFECTS OF GROWTH ORIENTATION ON THE PROPERTIES OF STRAINED SEMICONDUCTOR QUANTUM WELL LASERS

M. Sc. Thesis

in

Physics Engineering
University of Gaziantep

97018

By
Murat ODUNCUOĞLU

January 2000

T.C. YÜKSEKÖĞRETİM KURULU
DOKÜMANTASYON MERKEZİ

Approval of the Graduate School of Natural and Applied Science.

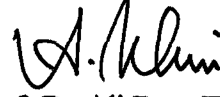

Assoc. Prof. Dr Ali Rıza TEKİN

Director

I certify that this thesis satisfies all the requirements as a thesis for the degree of Master of Science.

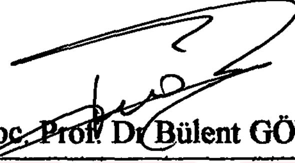

Assoc. Prof. Dr Bülent GÖNÜL

Chairman of the Department

I certify that I have read this thesis and that my opinion it is fully adequate, in scope and quality, as a thesis for the degree of Master of Science.

Assoc. Prof. Dr Beşire GÖNÜL

Supervisor

Examining Committee in Charge :

Assoc. Prof. Dr Bülent GÖNÜL (Chairman)

Assoc. Prof. Dr Beşire GÖNÜL

Assist. Prof. Dr A. Necmeddin YAZICI

ABSTRACT

EFFECTS OF GROWTH ORIENTATION ON THE PROPERTIES OF STRAINED SEMICONDUCTOR QUANTUM WELL LASERS

ODUNCUOĞLU Murat
M. Sc in Physics Engineering
Supervisor: Assoc. Prof. Dr Beşire GÖNÜL

January 2000, 77 Pages

The work described in this thesis investigates how strain and crystal orientation affect the band structure of quantum well lasers. The study provides a better understanding of the dependence of effective mass, strain-induced band-edge shift, change in the band-gaps and emission wavelengths on the substrate orientation. A detailed calculation of the confined states considering the effects of well width, substrate orientation, piezoelectric field, band-offsets, transition strengths of allowed and forbidden transitions was carried out.

The lack of inversion symmetry in polar, zinc-blende crystals when grown on axes other than (001) leads to the formation of internal piezoelectric fields when such structures are strained. The built-in electric field modifies the electronic

structure and optical properties of the crystal. Recently, it has been suggested that piezoelectric quantum well lasers operated under forward bias could be used in an integrated laser. Design of such devices requires a knowledge of the behaviour of the quantum well structure as a function of carrier and current densities. It has been shown previously that maximum gain reduces with increasing piezoelectric field. We explain the reductions of maximum gain in the presence of internal piezoelectric fields considering the overlaps between envelope functions of the confined states.

Keywords: Quantum wells, growth orientation, strain, critical thickness, optical gain

ÖZET

BÜYÜTME YÖNÜNÜN STRAIN UYGULANMIŞ YARIİLETKEN KUYU LAZERLERİNİN ÜZERİNDEKİ ETKİLERİ

ODUNCUOĞLU Murat
Yüksek Lisans Tezi
Fizik Mühendisliği
Tez Danışmanı: Doç. Dr Beşire GÖNÜL
Ocak 2000, 77 Sayfa

Tezde yapılmış olan bu çalışma birim uzama-kısalmanın ve kristalin büyütme yönünün kuantum kuyu lazerinin bant yapısını nasıl etkilediğini araştırır. Bu çalışma; etkin kütlenin, birim uzama kısalmanın yol açtığı bant kıyısındaki değişikliğin, yasak bant aralığındaki değişimin ve yayılma dalga boyunun büyütme yönüne bağlı olan değişimin daha iyi anlaşılmasını sağlar. Kuyu içerisine hapsolmuş izinli enerji seviyeleri; kuyu derinliği, genişliği, kristalin büyütme yönü, piezoelektrik alanı, izinli ve izinsiz geçişlerde geçiş şiddeti göz önüne alınarak detaylı bir şekilde hesaplandı.

Ters dönme simetrisine sahip olmayan zinc-blende gibi kristaller (001) yönünden farklı bir yönde büyütüldüğünde ve bunlara strain uygulandığında bu yapılarda piezoelektrik alanı oluşur. Oluşan bu elektrik alanı kristalin elektronik yapısını ve optik özelliklerini değiştirir. Son zamanlarda böyle bir yapıya sahip kuantum kuyusunun entegre lazer olarak kullanılabileceği ileri sürüldü. Bu tür cihazların tasarımı lazerin kazanç materyalinin taşıyıcı ve akım yoğunluğunun araştırılmasını gerektirir. Daha önce yapılan çalışma maksimum kazancın piezoelektrik alanı ile azaldığını göstermiştir. Biz bu çalışmada bu azalışın hapsolmuş seviyelerin overlap integrallerinin, piezoelektrik alanı ile değişimini inceleyerek açıklamaya çalıştık.

Anahtar Kelimeler: Kuantum kuyular, büyütme yönü, strain, kritik kalınlık, optik kazanç

ACKNOWLEDGEMENT

The author would like to express his thanks to his supervisor, Assoc. Prof. Dr Beşire GÖNÜL, for many stimulated discussions, guidance, encouragement, and suggestions in the construction of this work.

His special thanks also go to his family.

Dedicated to my son R. Emre

TABLE OF CONTENTS

ABSTRACT iii
ÖZET v
ACKNOWLEDGEMENT vii
TABLE OF CONTENTS viii
LIST OF TABLES x
LIST OF FIGURES xi

1. INTRODUCTION 1
2. THE ORIGIN OF QUANTUM WELLS AND STRAINED QUANTUM WELL LASERS
   2.1 Introduction 6
   2.2 Early Proposals 7
   2.3 The First Observations of Quantum Wells 8
   2.4 Quantum Well Laser 11
   2.5 Density of States (DOS) 13
      i. Three- Dimensional Density of States. 13
      ii. Two - Dimensional Density of States 15
   2.6 Strain Theory 18
   2.7 Strained Quantum Well 19

3. OPERATION PRINCIPLES OF SEMICONDUCTOR LASERS

3.1 Introduction 22
3.2 Electronic Transitions 23
3.3 Laser Threshold Current Density 26
3.4 Light-Current Curve 28

4. STRAINED QUANTUM WELL LASER STRUCTURES GROWN ON (111) GaAs

4.1 Introduction 30
4.2 Critical Thickness in Strained Layer Lasers 33
4.3 Orientation Dependence of Material Parameters 36
4.3.1 Effective Masses 36
4.3.2 Elastic Deformation and Strain-induced Band-edge Shift 38
4.3.3 Change in the Bandgaps and Emission Wavelengths for the two Orientations 41
4.3.4 Piezoelectric Effect 46
4.4 Energy Levels and Wavefunctions 49

5. GAIN IN QUANTUM WELL LASERS

5.1 Introduction 58
5.2 Gain Theory 58
i. Quantized Energy Levels and Carrier Densities 60
ii. Linear Gain 63
5.3 Linear Gain in (111) Oriented Strained Quantum Well Lasers 65

6. CONCLUSION AND FUTURE WORK 69

REFERENCES 71

APPENDIX A

A.1 Material Parameters 76

LIST OF TABLES

Table 4.1 Conduction-band edge effective mass $m_{\Gamma 6}$ and calculated hole effective masses for (001) and (111) orientations using Luttinger parameters from Molenkamp for GaAs and Lawaetz for InAs.

Table 4.2 Semiconductor properties of GaAs and InAs used in the present calculation. All parameters are from Landölt – Bornstein (Vol.17a, 1982) unless otherwise noted, for a see reference [22].

LIST OF FIGURES

Figure 2.1 The optical absorption spectra of bulk and quantum well heterostructures. [after Dingle et al., Ref. 17].

Figure 2.2 Schematic representation of the confined particle energy levels of electrons, heavy holes (dashed lines), and light holes (long dashes) in a quantum well.

Figure 2.3 Energy subbands and the two-dimensional DOS formed in a quantum well in the z-direction. In the x-y plane, the DOS is three-dimensional and is given by dashed curve.

Figure 2.4 Model diagram showing the density of states and carrier occupancy (shaded area) in (a) bulk (3D) and (b) quantum well structure (2D)

Figure 2.5 A schematic representation of the growth of (a) a compressively strained layer and in which the bulk lattice constant of the overlayer is larger than that of the substrate, and (b) the tensile strained layer in which the lattice constant of the overlayer is smaller than that of substrate. The overlayer must match the in-plane lattice constants of the substrate. Too large a mismatch may prevent epitaxially growth altogether or lead to fractures and undesirable effects.

Figure 2.6 Schematic diagram of energy bands in a semiconductor quantum well near the Brillouin zone center; unstrained (center), under biaxail compressive strain (right), and under tensile strain (left). $k_\perp$ levels represents the growth direction wavevector, while the $k_{||}$ represents the in-plane wavevector.

Figure 3.1 Schematic illustration of absorption, spontaneous emission and stimulated emission. In both spontaneous and stimulated emission processes an electron-hole pair recombine to generate a photon.

Figure 3.2 Light- Current (L - I) curve of a typical semiconductor laser.

Figure 4.1 Conduction, valence band edges and carrier wavefunctions for quantum wells grown along (001) and (111) oriented substrates.

Figure 4.2 Schematic diagram (a) of separate $In_xGa_{1-x}As$ and GaAs unit cells, (b) a single strained layer $In_xGa_{1-x}As$ structure, and (c) an inserted $In_xGa_{1-x}As$-GaAs strained layer structure. Shown for reference, as a dashed line is the original $In_xGa_{1-x}As$ cell shape.

Figure 4.3 Comparison of the critical thickness of a strained quantum well grown on (111) and (001) oriented substrates calculated as a function of indium composition, using the Matthews and Blakeslee model.

Figure 4.4 The heavy- hole and light-hole masses for both (001) and (111) orientation for the Indium content.

Figure 4.5 Illustration of the compression that results perpendicular to the growth direction for tension in the plane of the layers.

Figure 4.6 Illustration of strain decomposition for the case of biaxial compression in a cubic crystal. The unit cell on the left compresses in the plane ("||" direction) by a fractional amount, $\varepsilon_{||}$, giving an increase in "height" $\varepsilon_{\perp}$. The axial strain, ε_{ax}, is the amount by which the crystal is extended in the "⊥" direction compered to the height it would have had (short dashed).

Figure 4.7 The shift in the heavy-hole valence band edge (ΔE_{hh}) and light hole valence band edge (ΔE_{lh}) with respect to the conduction band edge for (001) and (111) orientation as a function of In composition for $In_xGa_{1-x}As$-GaAs strained layers.

Figure 4.8 Schematic representation of the (a) bulk bandgap, (b) uniaxial bandgap energy, and (c) emission wavelength for $In_xGa_{1-x}As$ quantum well on (001) and (111) oriented GaAs substrates as a function of Indium composition.

Figure 4.9 Schematic diagram of the band structure modification for both (a) (111) and (c) (001) orientations.

Figure 4.10 Calculated magnitude of the strain induced electric field versus In composition x in an elastically deformed $In_xGa_{1-x}As$ strained layer grown on (111) GaAs substrates by taking e_{14} as linear interpolation of standard values of binary compounds (dashed line) and taking the fitted value of e_{14} (solid line).

Figure 4.11. Calculated quantized energy levels for the electrons for (001) growth.

Figure 4.12 The confined heavy- and light-hole states for (001) and (111) orientation as a function of well width.

Figure 4.13 Wavefunctions for the first confined electron state in conduction band and the first confined heavy-hole state in valence band in a quantum well in the presence of an internal piezoelectric field.

Figure 4.14 The confinement energies of both first electron- and hole-states as a function of piezoelectric field for different band-offsets (well-depths).

Figure 4.15 The amplitude of the confined energy level of first heavy-hole state, E_{hh1}, with increasing piezoelectric field for three different values of valence-band-offset, ΔE_v .

Figure 4.16. The shift in the confinement energies of the first heavy-hole state.

Figure 5.1 The coordinate system.

Figure 5.2 Conduction and valence (a) wells and quantized energy levels, and (b) subband structures and optical transition.

Figure 5.3 Calculated maximum gain versus injected carrier density for 0, 50, 100 and 150 kV/cm internal fields in 70 Å $In_{0.4}Ga_{0.6}As$ quantum well laser on a (111) GaAs substrate.

Figure 5.4 Calculated overlap integrals as a function of piezoelectric fields for all allowed and forbidden transitions.

CHAPTER 1

INTRODUCTION

Semiconductor diode lasers are the key components at the heart of many new high volume products such as compact disc players, laser printers, and fiber optic communication links. Most of the diode lasers used in these products are of the double heterojunction design in which the laser power is generated by electron-hole recombination in an active layer about 100 to 200 nm thick. This double heterojunction design, perfected in the late 1970s and early 1980s, is now giving away to a more complex design in which the active layer is about an order of magnitude thinner than in the double heterojunction design. As the active layer thins down to the 10 nm regime, the distribution of low energy, wave-like states available for electrons and holes confined to the active layer (potential well) changes from quasi-continuous to discrete. Since laser action is derived by stimulating electron-hole recombination between these discrete (quantum well) states, devices with this active layer design are called quantum well lasers.

The first ideas that quantum effects might be utilised to make better diode lasers were generated in the early 1970s. The inspiration for these ideas came from the new field of integrated optics, which was just starting to gather momentum at the time. While considering GaAs/AlGaAs waveguides, where refractive index differences are utilised to confine photons on discrete modes, Charles B. Henry from Bell Laboratories realised that the bandgap differences between these materials might also be used to confine electrons on discrete modes or quantum states. He then went on to predict that the spectral absorption profile of thin GaAs

layers sandwiched between layers of AlGaAs should show a series of bumps characteristic of the quantum well state distribution. The successful demonstration of this effect by R. Dingle using material grown by W. Weigmann led to further predictions suggesting that diode lasers made with quantum wells should have performance characteristics superior to those of the standard double heterojunction lasers being made at that time. It was not until the late 1970s and early 1980s that reports began to appear claiming that high performance diode lasers incorporating GaAs/AlGaAs quantum wells could in fact be realised. A review of the state of the quantum well laser art up to about 1985, written by W. T. Tsang, can be found in Volume 24 of the Semiconductor and Semimetals Series published by Academic Press in 1987 (edited by Raymond Dingle).

Since 1985, the published literature on quantum well lasers has increased enormously. Perhaps the most important development that has come out of all of this new work is the realisation that quantum well lasers with built-in strain can have performance characteristics, including reliability, that are substantially superior to unstrained devices. First theoretical studies on strained quantum wells show that compressive strain enhances heavy hole-light hole (HH–LH) splitting and reduces the in-plane effective mass, resulting in reduced threshold current and increased differential gain because of the reduced density of states at the band edge [1]. These laser diodes have been traditionally been grown on (001) substrates because of the wide range of growth conditions which result in good epitaxial layer quality on this crystalline orientation. However, optical and electrical properties can also be improved an orientations other than (001). Recently, much attention has been paid to epitaxial growth on (111) GaAs substrates in particular, because of attractive properties. The threshold current of GaAs / AlGaAs quantum well lasers can be lowered significantly by using the (111) face [2,3], which is an obvious advantage. The large heavy-hole effective mass along the growth direction in (111) GaAs / AlGaAs quantum well structure gives rise to a 50% enhancement of the quantum efficiency of interband transitions [2,4]. As a result, reduction of the threshold current in a heterostructure laser fabricated from a GaAs / AlGaAs quantum well structure grown on a GaAs (111) substrate has been achieved [2]. In addition, the critical thickness of strained InGaAs layers grown on (111) GaAs is about twice that of a (001) [5]. This enhancement of the critical layer thickness

allows an increase of In content in strained InGaAs quantum well lasers, in turn allowing longer-wavelength lasers to be grown on (111) GaAs than on (001) GaAs. More interestingly, a net displacement of the positive and negative charges can be generated in a strained quantum well grown on (111) substrate due to the lack of inversion symmetry in the zinc-blende structure [6]. As a result, an internal electric field can be produced due to the piezoelectric effect [7]. Some novel nonlinear optoelectronic devices, such as self-electro-optic-effect devices (SEED's) [8] and optical switches, were consequently proposed by using blue-shifted electroabsorption [7] and large optical nonlinearity resulting from the screening of the internal electric field, respectively [9]. It is difficult; however, to grow an InGaAs strained quantum well laser on (111) GaAs. Therefore, the optical properties of quantum well structures are believed to change with their crystal orientation, and therefore, the substrate orientation is a new parameter in the engineering of strain-induced band structure modification to optimise laser performance.

Chapter 2 presents the origin and first observation of quantum wells with the ability to grow different semiconductor layers epitaxially with the atomic scale precision in thickness, the material bandgap can be designed to confine electron motion along the growth direction. This quantum confinement of the electron significantly alters the band structure of the semiconductor altering almost every property of the material to one degree or another. The problems with a homojunction device which can be overcome with a heterostructure are poor optical confinement, population inversion and poor carrier confinement and all three of which lead to a high operating current. The concepts of quantum well lasers, strain in semiconductor heterostructures and strained quantum well laser are briefly introduced. The single most useful quantum-confined structure in optoelectronics is arguably the quantum well. The semiconductor quantum well is a thin layer (~10 nm) of a small gap semiconductor which sandwiched between two layers of higher band gap compounds acting as barriers which confines the carriers into the quantum well. Strained layer quantum wells are generally obtained by coherent growth of lattice-mismatched compounds, using modern growth techniques. A comparison of the three- and two-dimensional density of states is presented and a 2D density of states for an idealised quantum well is illustrated.

Finally, strain theory, the introduction of strain into the quantum well lasers and the modifications in the energy band diagrams is summarised.

Chapter 3 starts by reviewing the basic laser mechanism relevant to semiconductor devices. The ideas of optical absorption, spontaneous and stimulated emission are provided. The Bernard-Duraffourg condition is first described and related to the transparency carrier density, and is then extended to explain the concept of net stimulated emission rate, optical gain and the threshold gain condition for a Farby-Perot type laser device. The theory of the threshold current is explained and developed to include both the radiative and non-radiative contributions important in lasers.

Semiconductor heterostructure are ideal quantum well structures are ideal quantum structure to explore various interesting physical phenomena and novel device applications. Electronic states of the quantum well can be engineered by changing the material combination, alloy composition, layer thickness, doping level, and even the substrate orientation. Previous research has mainly been conducted on heterostructures grown on (001) substrates. It has been demonstrated recently however that compound semiconductor heterostructures grown on (111) substrates have some novel physical properties. The large heavy-hole effective mass along the growth direction in (111) GaAs / AlGaAs quantum wells gives rise to a 50-fold enhancement of the quantum efficiency of interband transitions. As a result, reduction of the threshold current in heterostructure laser fabricated from a GaAs / AlGaAs quantum well structure grown on a GaAs (111) substrate has been achieved. More interestingly, a net displacement of the positive and negative charges can be generated in a strained quantum well grown on a (111) substrate due to the lack of inversion symmetry in the zinc-blende structure. As a result, an internal electric field can be produced due to the piezoelectric effect. The work presented in chapter 4 is intended to explore the quantum size effect of the (111) and heterostructures, and to provide a better understanding of the dependence of the optical properties on the substrate orientation.

First part of the chapter 5 presents the linear gain calculations for quantum well lasers. In the second part of this chapter we tried to explain the earlier results of peak gain calculations for (111) oriented InGaAs / GaAs quantum wells by means of their transition strengths.

Finally, chapter 6 summarizes our conclusions from this study and presents the future work.

CHAPTER 2

THE ORIGIN OF QUANTUM WELLS
AND
STRAINED QUANTUM WELL LASERS

2.1 Introduction

Semiconductor lasers are attractive for research because they are both physically very interesting and technologically important. This is especially true of quantum well lasers. Quantum well technology allows the crystal growth for the first time to control the range, depth, and arrangement of quantum mechanical potential wells. This can be used not only to demonstrate examples of elementary quantum mechanics, but to make a very good lasers. In the last decade, the importance of quantum well laser has steadily grown until today it is preferred for most semiconductor laser applications. While the first quantum well lasers operated at a wavelength near 0.8 μm, they have now been demonstrated from the visible through the infrared (0.49-10 μm).

This growing popularity is because, in almost every respect, the quantum well laser is somewhat better than conventional lasers with bulk active layers. One obvious advantage is the ability to vary the lasing wavelength merely by changing

the width of the quantum well. A more fundamental advantage is that the quantum well laser delivers more gain per injected carrier than conventional lasers, which results in lower threshold currents. Because the injected carriers are in large measure responsible for internal losses, quantum well lasers, which require fewer injected carriers, are more efficient and can generate more power than the conventional lasers. Another advantage is that quantum well lasers deliver gain with less change in refractive index than bulk lasers. Both lower internal loss and lower refractive index change result in quantum well lasers having narrower linewidth than conventional lasers. The splitting of the light- and heavy-hole valence bands by spatial quantization as well as the ability to grow quantum wells with compressive and tensile strain results in greater control over the optical polarisation than in bulk lasers. The differential gain, gain per injected electron, is greater in properly designed multi-quantum well lasers and should lead to higher speed than for bulk lasers.

In view of the great interest in this laser, it seems appropriate to look back and review its origin. In this chapter we will trace the history of the quantum well laser from the first calculations and experiments on quantum wells to the first quantum well lasers of high performance.

2.2 Early Proposals

Modern semiconductor lasers incorporate a heterostructure in which the

of interfaces and depletion effects, the heterostructure acts as a potential well for electrons in the conduction band and holes in the valence band. It was natural for those concerned with heterostructures to try to model what would happen when these layers became extremely thin and spatial quantization occurred. The first work in this direction was that of L. Esaki and R. Tsu of IBM in 1970 [16], who considered carrier transport in a superlattice, an additional periodic potential formed in a semiconductor by doping or alloy composition and having a period of order 100 Å. They concluded that a parabolic band would break into mini-bands separated by small forbidden gaps and having Brillouin zones associated with this period.

2.3 The First Observations of Quantum Wells

In 1972, Charles Henry realised that a heterostructure is a waveguide for electrons. On reflection, it was clear that there is a complete analogy between the confinement of light by a slap waveguide and confinement of electrons by the potential well that is formed from the difference in bandgaps in a heterostructure. This then led him to think that there should be discrete modes (levels) in the quantum well, and a simple estimate showed that when the heterostructure was as thin as several hundred angstrom units, the electron levels would be split apart by tens of milli-electron volts. He then calculated that how this quantisation would alter the optical absorption, considering only that noninteracting electrons are bound in the well. His conclusion was that instead of the absorption increasing smoothly as the square root of energy, the absorption edge of a thin heterostructure would appear as a series of steps.

In early 1973, R. Dingle and W. Wiegmann [17] grew GaAs/AlGaAs hetero-structure by molecular beam epitaxy to look for steps associated with quantized levels in the absorption edge. The results of these experiments were the remarkable spectra shown in Fig.2.1. The steps in the absorption edge were observed. Associated with each step there was a strong exciton peak.

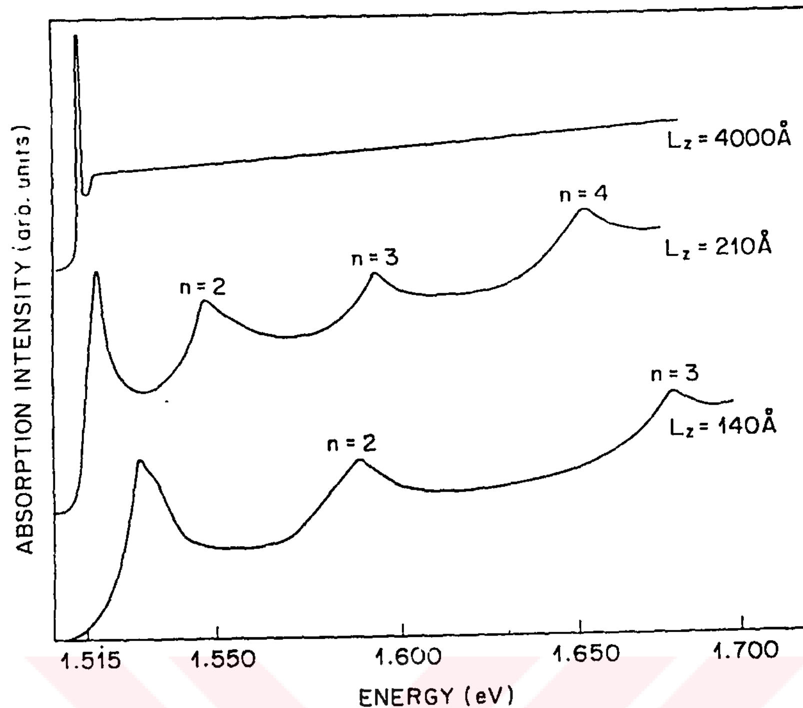

Figure 2.1 The optical absorption spectra of bulk and quantum well heterostructures. [17].

A heterojunction is a junction in a single crystal between two dissimilar semiconductors. The distinguishing difference is generally the band structure, and the most important feature of the band structure is the energy gap. All the electronic and the optical properties of semiconductor devices are dependent upon the band structure. The band structure of semiconductors can be changed and over the last decade this has become one of the driving force in semiconductor physics. Heterostructures are able to improve the performance of semiconductor devices because they permit the device designer to locally modify the energy-band structure of the semiconductor and so control the motion of the charge carriers. The ability to modify the band structure provides a new and exiting dimension in device design. Many physical phenomena can modify the electronic band structure, and involves:

i. Alloying of two or more semiconductors;

ii. Use of heterostructures to cause quantum confinement or formation of "superlattices";

iii. Use of built–strain via lattice mismatched epitaxy.

These three concepts are increasingly being used for improved performance in electronic and optical devices and their importance is expected to become greater with each passing year.

Most semiconductor optoelectronic devices, other than silicon photo dedectors, are made from heterostructures. They are practically important semiconductor optoelectronic devices for at least four reasons:

I. Use of different materials allows us to control where the electrons and holes go into devices, which is particularly useful for making efficient lasers;

II. Different materials have different refractive indices, which allows us to make waveguides and mirror structures out of the same materials used to make the optoelectronic devices themselves;

III. One can make structures in which only certain parts absorb or emit light at the wavelengths of interest (the other parts being transparent);

IV. In advanced optoelectronic devices, the different materials allow us to quantum-confine the electrons and holes in very thin layers, enabling quantum-mechanically engineered devices.

An understanding of the physical properties of heterostructures is essential to their use in devices. The energy-band alignment is the most fundamental property of a heterojunction and it determines the usefulness of various material combinations for different device applications. The band profile of a heterostructure is determined by the combined effects of heterojunction discontinuities and carrier screening and it determines many of the electrical properties of the structure.

If a heterostructure is made between two materials for which there exists a continuum of solid solutions, such as between GaAs and AlAs (as $Al_xGa_{1-x}As$ exists for all x such that $0<x<1$), the chemical transition need not occur abruptly. That is, the composition parameter x might be some continuous function of the position.

2.4 Quantum Well Laser

A double heterostructure laser consists of n active layer sandwiched between two higher-gap cladding layers. The active-layer thickness is typically in the range of 0.1-0.3 μm. In the last few years, double-heterostructure lasers with an active-layer thickness of ~10 nm have been fabricated. The carrier (electron or hole) motion normal to the active layer in these structures is restricted. As a result, the kinetic energy of carriers moving in that direction is quantized into discrete energy levels similar to the well-known quantum-mechanical problem of the one-dimensional potential well, and hence these lasers are called quantum well lasers.

When the thickness of the active region (or any low-gap semiconductor layer confined between higher-gap semiconductors) becomes comparable to the de Broglie wavelength ($\lambda = h/p$), quantum-mechanical effects are expected to occur. These effects are observed in the absorption and emission characteristics (including phenomena such as tunnelling) [10-16].

A carrier (electron or hole) in a double heterostructure is confined within a three dimensional potential well. The energy levels of such carriers are obtained by separating the system Hamiltonian into three parts, corresponding to the kinetic energies in the x, y, and z directions. When the thickness of the heterostructure (L_z) is comparable to the de Broglie wavelength, the kinetic energy corresponding to the carrier motion along the z direction is quantized. Along the x, and y directions, the energy levels form a continuum states given by

$$E = \frac{\hbar^2}{2m}(k_x{}^2 + k_y{}^2) \qquad (2.1)$$

where m is the effective mass of the carrier and k_x and k_y are the wavevector components along the x and y directions, respectively. Thus the electrons or holes in a quantum well may be viewed as forming a two-dimensional Fermi gas.

The potential well for electrons and holes in a double heterostructure depends on the materials involved. The following values for the conduction band (ΔE_c) and valence-band (ΔE_v) discontinuities are found experimentally [18a] for GaAs-AlGaAs double heterostructures:

$$\Delta E_c / \Delta E = 0.67 \pm 0.01, \quad (2.2)$$

$$\Delta E_v / \Delta E = 0.33 \pm 0.01, \quad (2.3)$$

where ΔE is the band gap difference between two confining and active layers. A knowledge of ΔE_c and ΔE_v is necessary in order to accurately calculate the energy levels. For an InGaAsP-InP double heterostructure, values obtained are [18b]

$$\Delta E_c / \Delta E = 0.39 \pm 0.01, \quad (2.4)$$

$$\Delta E_v / \Delta E = 0.61 \pm 0.01. \quad (2.5)$$

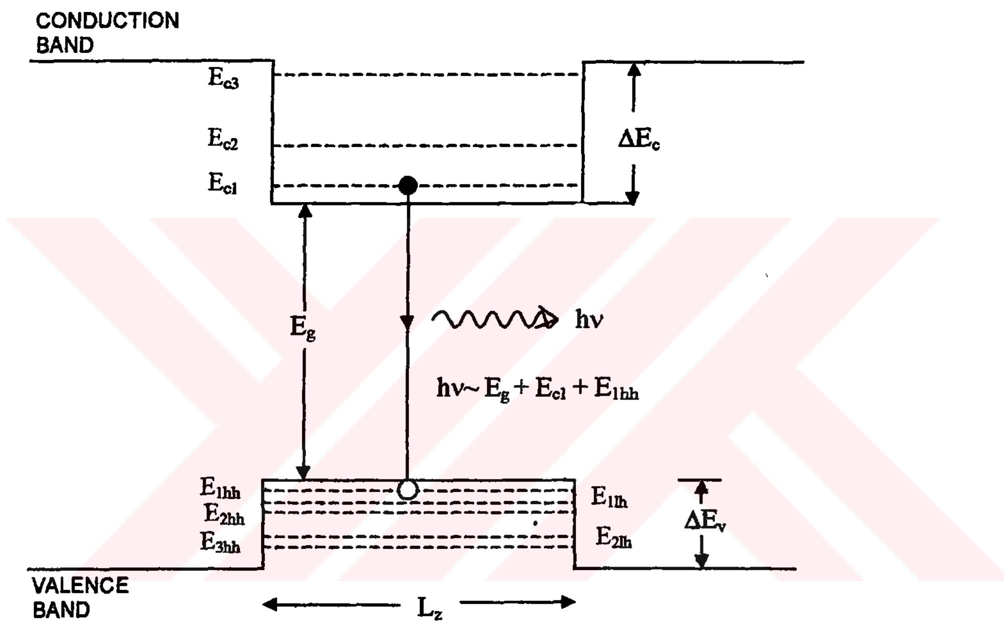

Figure 2.2 Schematic representation of the confined particle energy levels of electrons, heavy holes (dashed lines), and light holes (long dashes) in a quantum well.

Taking into account discrete states along the z direction and continuous states along the x and y directions, the energy eigenvalues for a particle confined in the quantum well are

$$E(n,k_x,k_y) = E_n + \frac{\hbar^2}{2m_n^*}(k_x^2 + k_y^2) \quad (2.6)$$

where E_n is the n th confined particle energy level for this level. Fig.2.2 shows schematically the energy levels E_n of electrons and holes confined within a quantum well. The confined particle energy levels E_n are denoted by E_{c1}, E_{c2} and E_{c3} for electrons; E_{1hh}, E_{2hh}, E_{3hh} for heavy holes; and E_{1lh}, and E_{2lh} for light holes.

2.5 Density of States (DOS)

Free carriers, electrons and holes, are essential for the operation of active semiconductor devices. These free carriers can be introduced in a semiconductor either by a process of doping or electrical injection. Depending on the temperature of the crystal, the carriers are distributed in energy in the dopant energy levels and respective bands. The number of carriers at any energy level will then depend on the number of available states at that energy and the energy distribution of the carriers. The two important functions that determine carrier distribution in a semiconductor are the energy distribution function and the density of states function.

To determine the density of states, the existing electronic states in the crystal must be determined. The density of state (DOS) functions N(E)dE gives the number of available quantum states in the energy interval between E and E+dE. In what follows, we will present an expression for N(E), first for the case of a three-dimensional bulk semiconductor, and then for the case of a two-dimensional density of carriers, as found in a quantum well.

i) Three- Dimensional Density of States.

Consider a cubic region of the crystal with dimensions L along the three perpendicular directions and impose the condition that the electron wave functions become zero at the boundaries of the cube defined by values of x, y, and z equal to 0 and L. The boundary conditions are satisfied by a wavefunction of the form

$$\psi_k(r) = U_k(r)\, Sin(k_x x) Sin(k_y y) Sin(k_z z)\,, \qquad (2.7)$$

where $U_k(r)$ has the periodicity of the crystal lattice and the boundary conditions lend to

$$k_x L = 2\pi n_1,$$
$$k_y L = 2\pi n_2,$$
$$k_z L = 2\pi n_3, \tag{2.8}$$

where n_1, n_2 and n_3 are integers. Therefore, each allowed value of k with coordinates k_x, k_y and k_z occupies a volume $(2\pi / L)^3$, in k-space. In other word, the density of allowed points in k-space is $V / (2\pi)^3$, where $V=L^3$ is the crystal volume.

Let's consider, the three dimensional DOS. The volume in k-space defined by vectors k and k+dk is $4 \pi k^2 dk$. Hence, the total number of states with k-values between k ands k+dk is

$$dN = 4\pi V k^2 dk / (2\pi)^3. \tag{2.9}$$

Taking into account the two possible values of spin;

$$dN = 8\pi V k^2 dk / (2\pi)^3. \tag{2.10}$$

For electrons in the conduction band of a semiconductor

$$k^2 = \frac{2m_{\|}(E - E_c)}{\hbar^2} \tag{2.11}$$

which, by differentiation leads to

$$2kdk = \frac{2m_{\|} dE}{\hbar^2} \tag{2.12}$$

Substitution of Eqn.(2.11) and Eqn.(2.12) into Eqn. (2.10) results

$$dN = \frac{8\pi V \left[2m_{\|}(E - E_c)/\hbar^2\right]\left(\dfrac{2m_{\|} dE}{\hbar^2}\right)}{\{2\left[2m_{\|}(E - E_e)/\hbar^2\right]^{1/2}(2\pi)^3\}} . \tag{2.13}$$

and for unit volume of the crystal,

$$N(E)dE = M_c \frac{\sqrt{2}}{\pi^2}\left(\frac{m_{\|}}{\hbar^2}\right)^{3/2}(E-E_c)^{1/2}dE. \quad (2.14)$$

Here, M_c is the number of equivalent minima in conduction band. A similar equation holds for the DOS in the valence band.

ii) Two - Dimensional Density of States

For the two-dimensional case, the DOS for each subband in a quantum well can be calculated, as follows. As in the there dimensional case of,

$$k_x = \frac{2\pi}{L_x}, k_y = \frac{2\pi}{L_y}, k_z = \frac{2\pi}{L_z}. \quad (2.15)$$

It is assumed that $L_z \ll L_x$, L_y. In a quantum well L_z represents the width of the well. Therefore, each allowed value of k, or mode, occupies a volume in k-space equal to $(2\pi)^3 / L_xL_yL_z$. In present case the number of modes included between k and k+dk keeping $k_z = \pi / L_z$ constant must be determined. The mode numbers can be treated as a continuos variables in the k_x - k_y plane. As before, the density of allowed points in k-space equals $L_xL_yL_z / (2\pi)^3$. The volume in k space between k and k+dk is $2\pi\, k_{\|}\, dk_{\|}\, (2\pi / L_z)$, where $k_{\|}$ is the wavevector in the k_x - k_y plane. However, since

$$k^2 = \left(\frac{2\pi}{L_z}\right)^2 + k_{\|}^2. \quad (2.16)$$

It follows that

$$k\,dk = k_{\|}\,dk_{\|}. \quad (2.17)$$

The total number of states between k and $k\,dk$ is

$$dN = 2\left[\frac{L_x L_y L_z}{(2\pi)^3} 2\pi\, k\, dk\left(\frac{2\pi}{L_z}\right)\right]. \tag{2.18}$$

which takes into account the two possible spin values. On simplification,

$$dN = (L_x L_y L_z)\frac{1}{\pi^2} kdk(\frac{\pi}{L_z}). \tag{2.19}$$

In this case,

$$k^2 = \frac{2m_{\parallel}(E - E_n)}{\hbar^2}, n = 1,2,... \tag{2.20}$$

On substitution in Equation (2.19) the density of states in the energy interval dE is

$$N(E)dE = \frac{m_{\parallel}}{\pi\hbar^2 L_z} dE \tag{2.21}$$

provided $E > E_n = [\hbar(\pi / L_z)]^2 / 2 m_{\parallel}$, (n = 1). The two dimensional density of states is then

$$N(E)dE = \frac{m_{\parallel}}{\pi\hbar^2} dE. \tag{2.22}$$

Therefore, each of the two-dimensional bands gives to a band density of states that is independent of energy.

As can be seen from Fig.2.3, the states of the first subband overlap with the states of the second subband for energies larger than the second subband level and so on. As a result, the cumulative DOS for a series subbands will be step-like in character.

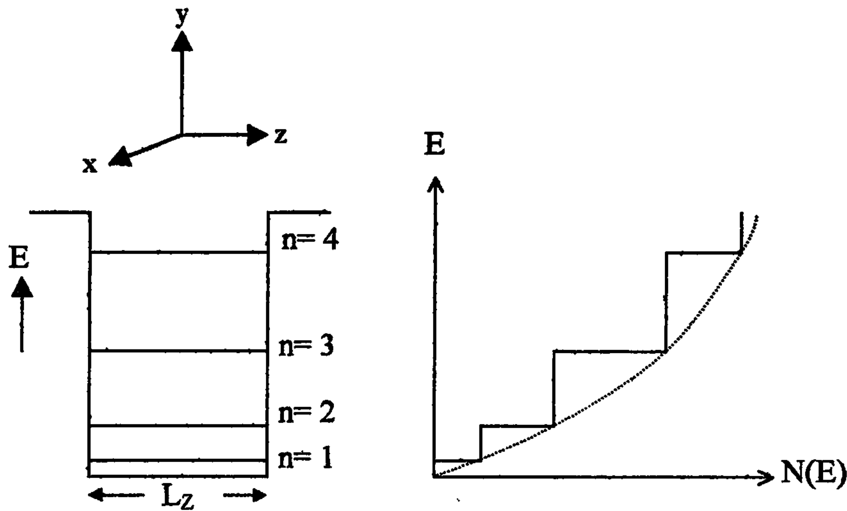

Figure 2.3 Energy subbands and the two-dimensional DOS formed in a quantum well in the z-direction. In the x-y plane, the DOS is three-dimensional and is given by dashed curve.

The density of states in bulk materials increases with energy as $E^{1/2}$ and is vanishing at the band edges. As a result, only a small fraction of the carriers populate the lowest states (shaded area) and the injected electrons and holes don't take the full advantage of the Fermi distribution (see Figure 2.4.a).

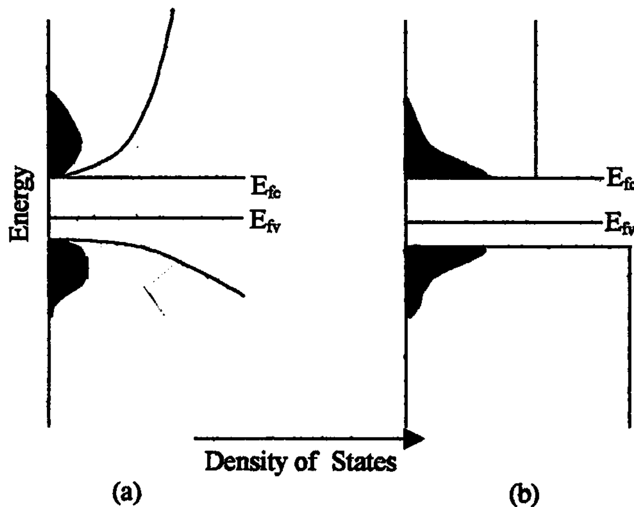

Figure 2.4 Model diagram showing the density of states and carrier occupancy (shaded area) in (a) bulk (3D) and (b) quantum well structure (2D)

The majority of direct (no change in momentum) radiative transitions in a laser take place via carriers in states close to the conduction and valence band-edges. Thus, the three dimensional (3D) bulk structure is highly inefficient since there are very few carriers close to the band-edge to take place in radiative recombination. This is not the case in two dimensional (2D) systems where the DOS is a step-like functions of energy and the peak in the injected carrier distribution is at the band edges. The usual parabolic form of the conduction and valence band density of states functions now to be replaced by a discrete levels, each corresponding to a constant density of states per unit area.

This more favourable shape of DOS is the chief reason why quantum well lasers have been predicted to have improved characteristics compered to their bulk counterparts. Nevertheless, the idealised quantum-well DOS illustrated in Fig.2.4.b is not yet the best case, because of the large valence band DOS. One can further improve the laser characteristics and in particular the gain by reducing the DOS in the valence band by incorporation of strain. There are then no allowed electron states below first excited state. When an electron and hole recombine $\Delta n=0$; an example is n=1 electrons can only recombine with n=1 holes. This illustrates the first important point about quantum well lasers; a large number of electrons all of the same energy can recombine with a similar number block of holes. Contrast with the bulk effect; where recombining carriers are distributed in energy over a parabolically varying density of states. Therefore, a quantum well laser should give much more narrower output wavelength. In a quantum well structure where we have an effectively a two-dimensional density of states, the electrons are spread over a smaller energy range with relatively high densities at the band edge. This situation implies that population inversion is easier to achieve in a quantum well laser.

2.6 Strain Theory

Semiconductor heterostructures can be grown epitaxially with two materials that are not perfectly lattice-matched, provided this mismatch is not to large.

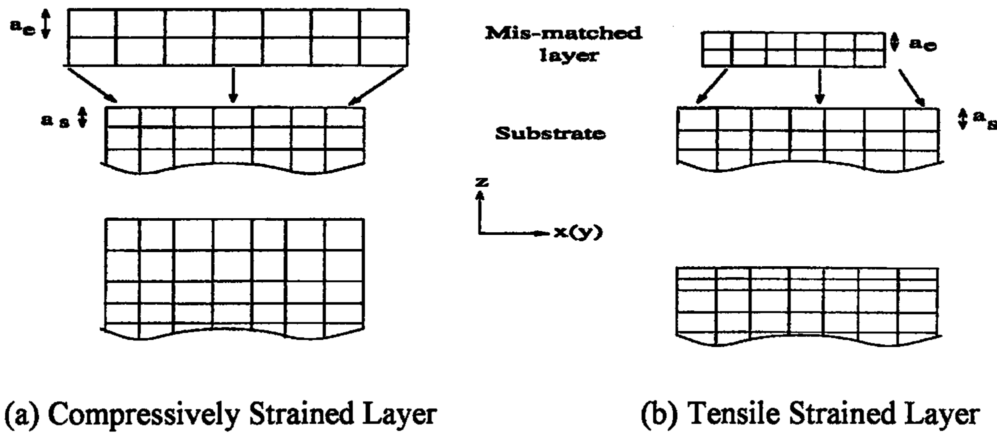

(a) Compressively Strained Layer (b) Tensile Strained Layer

Figure 2.5 A schematic representation of the growth of (a) a compressively strained layer and in which the bulk lattice constant of the overlayer is larger than that of the substrate, and (b) the tensile strained layer in which the lattice constant of the overlayer is smaller than that of substrate. The overlayer must match the in-plane lattice constants of the substrate. Too large a mismatch may prevent epitaxially growth altogether or lead to fractures and undesirable effects.

The semiconductor epilayer is biaxially strained in the plane of substrate, by an amount $\varepsilon_{\|}$, and uniaxially strained in the perpendicular direction, by an amount $\varepsilon_{\perp}$. For a thick substrate, the in plane strain of the epilayer is determined from the bulk lattice constants of the substrate material, a_s, and the layer material, a_e:

$$\varepsilon_{\|} = \frac{a_s}{a_e} - 1, \tag{2.23}$$

For a $a_e > a_s$, i.e. $\varepsilon_{\|} < 0$, the epitaxial layer is under biaxial compressive strain, while for $a_e < a_s$, the strain is tensile.

2.7 Strained Quantum Well

It is now possible to grow high quality strained layer structures, in which the quantum well (QW) layer is composed of semiconductor which would normally have a significantly different lattice constant to that of the barrier material.

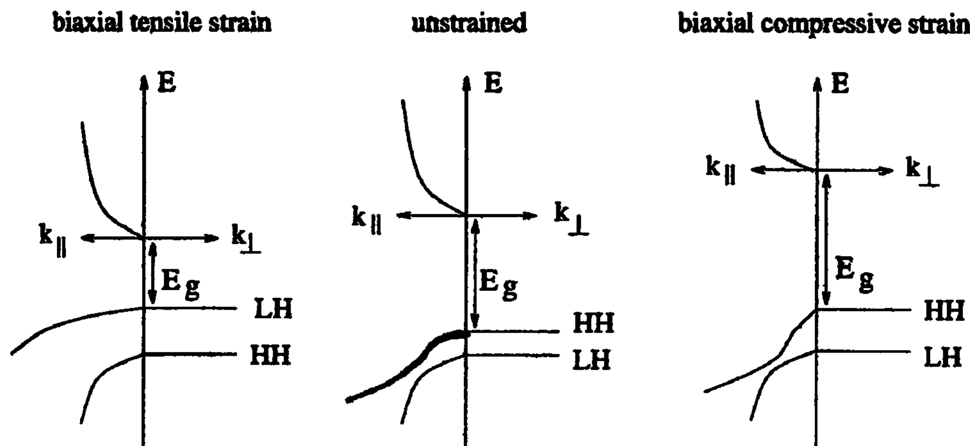

Figure 2.6 Schematic diagram of energy bands in a semiconductor quantum well near the Brillouin zone center; unstrained (center), under biaxail compressive strain (right), and under tensile strain (left). $k_{\perp}$ levels represents the growth direction wavevector, while the $k_{||}$ represents the in-plane wavevector.

The lattice mismatch is accommodated by tetragonal distortion of the quantum well layer, giving a built-in axial strain. This axial strain splits the degeneracy of the light- and heavy-hole zone-centre states, accessing a wide range of subband structures, including the possibility of the highest valence subband being light-hole-like, of significant benefit for semiconductor lasers. Since the strain can alter the heavy-hole, light-hole separation and hence the band occupation at threshold, it is possible to tailor the emission polarisation of the laser light.

Fig.2.6 is a schematic diagram of the energy bands in a zinc-blende semiconductor with combined quantum confinement and strain effects. The effect of quantum confinement on the ground state energy levels in a QW is indicated by the horizontal lines in the direction perpendicular to the epitaxial layer. In the unstrained case (centre of Fig.2.6), the quantum confinement effect alone results in the heavy-hole state being the highest valence band state and the energy difference between the light hole and heavy-hole bands varies with the depth and width L_z of the wells. The lowest energy transition which dominates in the optical spectra of such structure is from conduction band to the highest valence band state. In addition to altering the bandgap energy and shapes of the valence bands, biaxial

strain also lifts the light- and heavy-hole degeneracy at the zone center of the bulk semiconductors. Compressive strain increases the band gap and puts the heavy-hole band above the light-hole band, which is similar to the effect of quantum confinement. Therefore, a combination of compressive strain and quantum effects maintains the position of the heavy-hole as the highest valence band state (right side of the Fig.2.6) with a reduced heavy-hole subband mass along $k_{||}$ direction. On the other hand, tensile strain decreases the bandgap and can lift the light-hole above the heavy-hole (left side of Fig.2.6), which is opposite to the quantum confinement effect. Then, the lowest energy optical transitions are between the conduction band and the light-hole band. Under tensile strain, the mass along growth direction is reduced leading a large splitting between the light-hole subband in the quantum well structure. Thus a combination of the tensile-strain and quantum confinement results in either the heavy-hole being the highest valence band state, degenerate light-hole and heavy-hole states, or the light-hole being the highest state, depending on the relative strengths of the two effects.

CHAPTER 3

OPERATION PRINCIPLES OF SEMICONDUCTOR LASERS

3.1 Introduction

This chapter briefly examines the fundamental theory necessary to provide an adequate description of semiconductor lasers relevant to the work described in this thesis. A brief introduction to semiconductor laser theory is presented, covering the basic concepts in the remainder of the thesis. The ideas of optical absorption, spontaneous and stimulated emission, the density of states and the threshold current are introduced.

Laser light is distinguishable from naturally occurring light by its coherent properties and high brightness. Any laser can be seen as cavity containing

i) a gain medium capable of amplifying light and providing spontaneous emission noise input and,

ii) mirrors at the opposite ends for providing optical feedback.

The gain medium has electronic energy levels, some of which are completely saturated with electrons, other particularly populated while the rest are empty. At equilibrium, electrons populate the energy levels in decreasing order, starting from the lowest level and going to higher ones. Laser action in semiconductors involves the band structure. The electronic transitions that take place between the bands in a semiconductor laser play a similar role to the transitions between individual pairs

of electronic states in a two level laser system, although the actual electronic structure in semiconductor is much more complex. In both cases light can interact with the medium in three different ways, namely absorption, stimulated emission and spontaneous emission.

3.2 Electronic Transitions

In 1917, Einstein described the process of stimulated emission. In any material, during thermal equilibrium the number of particles in the excited state is very small and is negligible. Absorption occurs when incoming photon excites an electron in the valence band to the conduction band. The electron gains energy leading to the photon being absorbed or lost. In stimulated emission process, Einstein's contribution was to show that, a photon interacts with an electron in the conduction band stimulating the electron to recombine with a hole in the valence band and emits a second photon. The emitted photon has the same phase and frequency as the stimulating photon. In both cases, the energy of the incoming photon should be exactly equal to the energy difference between the two bands for the mechanism to take place. Finally when an electron in the conduction band finds an empty state or hole in the valence band, it spontaneously recombines with a hole in the valence band giving off a photon without the help of another as in stimulated emission.

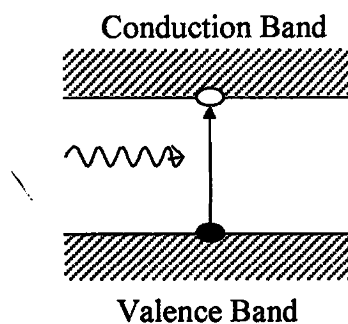

(a) Absorption

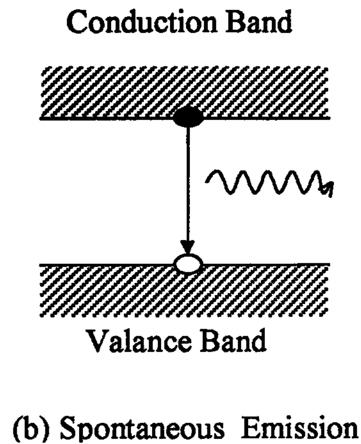

(b) Spontaneous Emission

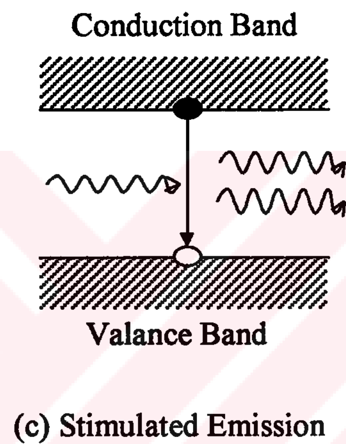

(c) Stimulated Emission

Figure 3.1 Schematic illustration of absorption, spontaneous emission and stimulated emission. In both spontaneous and stimulated emission processes an electron-hole pair recombine to generate a photon.

Spontaneous emission is just like radioactive decay, with less energetic by products, an atom in an excited state has a finite probability of decay per unit time, a decay probability characteristic of each atomic state. In this case, photons are emitted in random directions with no phase relation among them. In spontaneous emission, the energy of the emitted photon is equal to the to energy difference between two recombination levels.

The ground- state or lower energy level and the excited-state or higher energy level are present in Fig.3.1. The particle of the material, which undergoes the

process of excitation, might be an atom, molecule, or ion depending on the laser material.

In an undoped, direct bandgap semiconductor in thermal equilibrium, the conduction band usually contains only a few filled states and the valence band a few empty states. Therefore, stimulated emission is a highly improbable process in the case of thermal equilibrium due to the insignificant population of electrons in the conduction band. In order to increase the probability of stimulated emission, one has to increase the number of electrons in the conduction band. This is normally achieved by electrical injection. As the number of electrons in the conduction band increases, a point is reached when a photon of energy $h\upsilon$ will have the same probability of causing stimulated emission as of being absorbed and this leads to the semiconductor becoming optically transparent. This condition for net stimulated emission is that first stated by Bernard and Duraffourg [19]

$$E_{fc} - E_{fv} > h\upsilon \tag{3.1}$$

where E_{fc} and E_{fv} are the quasi-Fermi levels in the conduction and valence bands, respectively. At the point $E = E_{fc} - E_{fv}$, the semiconductor is transparent, and the number of the injected carriers per unit volume at this point is known as the transparency carrier density. When the number of particles in the excited state is greater than the number of particles in the ground state, the material is in a state of "population inversion". Population inversion is a prerequisite for laser action. Having considered the pre-condition for lasing in a two-level system, that the population in the upper level must be greater than that in lower one, it is intuitively straight forward to transfer this idea to semiconductors; the population of electrons in the lower part of the conduction band must be greater than that in the higher part of the valence band. Energy can be transferred into a laser medium to achieve population inversion by several mechanisms including absorption of photon, collision between electrons (or sometimes ions) and species in the active medium, collisions among atoms and molecules in the active medium, recombination of free electrons with ionised atoms, recombination of current carriers in a semiconductor, chemical reactions producing excited species, and acceleration of electrons. When the electrical injection exceeds a critical value, population inversion is reached, in

which the rate of photon emission exceeds that of absorption. Stimulated emission dominates, the gain medium is then able to amplify the input light and exhibit optical gain, for photon with energies $E = h\upsilon$, between the band gap E_g and $E_{fc} - E_{fv}$, a range which can corresponds to a wide spectral band width (a few tens of nm). However, optical gain alone is not enough to operate a laser. The other necessary ingredient is optical feedback. The gain obtained in a single travel of an electromagnetic wave down a laser cavity is small, and so in order to increase the overall gain multiple passes of a wave must occur. This is achieved using mirrors placed at either end of the cavity. For semiconductor lasers, the cleaved ends of the crystal forming the device acts as the mirror. For typical InP- and GaAs-based lasers, the cleaved facets provide about 30% optical intensity reflection due to the differences between the refractive indices of the semiconductor and air.

3.3 Laser Threshold Current Density

Although stimulated emission can occur as soon as current is applied to a semiconductor laser, the laser does not emit coherent laser light until the number of injected carriers reaches a certain critical value, known as the threshold carrier density n_{th}. This is so because the stimulated emission has to compete against the absorption process in which electron-hole pairs are generated due to the photon absorption. The medium gain g_{th} at the threshold is obtained by stating that the optical wave intensity after a roundtrip in the cavity must stay equal, under the opposite actions of losses and gain. This can be written as

$$I_0 R_1 R_2 \exp [2 (\Gamma g_{th} - \alpha_{abs}) L] = I_0, \quad (3.2)$$

where R_1 and R_2 are the facet reflectivities, Γ is the confinement factor, which is a measure of overlap between the lasing mode, and active region cross section, L is the laser length and α_{abs} accounts for the optical losses. Solving Eq.(3.2) for g_{th}, we have

$$g_{th} = \frac{1}{\Gamma}\left[\alpha_{abs} - \frac{\ln(R_1 R_2)}{2L}\right]. \quad (3.3)$$

To a good approximation the peak gain in a bulk semiconductor varies more or less linearly with carrier density. Such a linear relation may be written as

$$g_{th} = \beta\,(n_{th} - n_{tr}), \tag{3.4}$$

where β is the differential gain with respect to carrier density and n_{tr} is the carrier density needed to reach transparency in the gain medium. The injected three dimensional carrier density can be related to the injection current density by

$$n = \frac{J\eta_i}{e\gamma_r L_z}, \tag{3.5}$$

where e is the electron charge, γ_r is the recombination rate, L_z is the active layer thickness and η_i is the quantum efficiency with which the injected carriers arrive in the active region and contribute to the inversion. Since n is inversely proportional to L_z, the gain in Eq.(3.4) increases as L_z decreases for a given current density. More specifically, solving Eq.(3.4) for n using the threshold gain of Eq.(3.3), the threshold injection current density is

$$J_{th} = \frac{e\gamma_r L_z}{\eta_i}\left(n_{tr} + \frac{\alpha_{abs} - \ln(R_1R_2)/2L}{\beta\Gamma}\right). \tag{3.6}$$

Therefore the threshold current density is a strong function of the active region thickness. Reduction of this thickness reduces the threshold current density proportionally, unless Γ is changed.

When the current flowing through a semiconductor laser is increased, charge carriers (electrons and holes) are injected into the active region, where they can recombine through radiative and nonradiative mechanism to produce a current through the laser and associated threshold current density J_{th},

$$J_{th} = J_{rad} + J_{nr} + J_{stim} \tag{3.7}$$

where J_{rad} is the radiative current density, and is primarily caused by recombination via spontaneous emission, J_{nr} is contribution to the current from non-radiative recombination, including recombination via defects and J_{stim} is the contribution due

to stimulated emission. The relative proportions of different contributions to the total current density are heavily dependent on both the optoelectronic properties of the active region material and the engineered laser design.

One of the advantages of narrow active region is the expectation of low threshold current densities. It is apparent that there is a minimum thickness needed to the active region to make it efficient in laser operation. A consideration of charge movement will show that the carrier density in a quantum well structure is given by

$$n = \frac{J}{e}\frac{\tau}{L_y} \tag{3.8}$$

where τ is the carrier lifetime, L_y is the width of the active region, J is the current density. There is a minimum value of J needed to overcome the losses produced around a cavity and hence cause gain.

3.4 Light-Current Curve

Figure 3.2 shows a typical output power versus injection current or L-I curve for a semiconductor laser. The light output from a laser displays an abrupt change in behaviour below the "threshold" condition and above this condition. Two distinct regions, see Fig.3.2, can be identified for the operation of the laser. When the injected current is small, the number of electrons and holes injected are small. As a result, the gain in the device is too small to overcome the cavity loss. The photons that are emitted are either absorbed in the cavity or lost to outside. Thus, in this regime there is no build-up of photons in the cavity. However, as the current increases, more carriers are injected into the device until eventually threshold condition is satisfied for some photon energy.

At threshold, gain equals loss and the photon numbers starts to build-up in the cavity. As the device is further biased beyond threshold, stimulated emission starts to occur and dominates the spontaneous emission. A low threshold is important because it reduces the input electrical power that is not converted into laser radiation. Over a narrow current range in the vicinity of the threshold current, the output power jumps by several orders of magnitude and the spectral width of

the emitted radiation narrows considerably because of the coherent nature of stimulated emission.

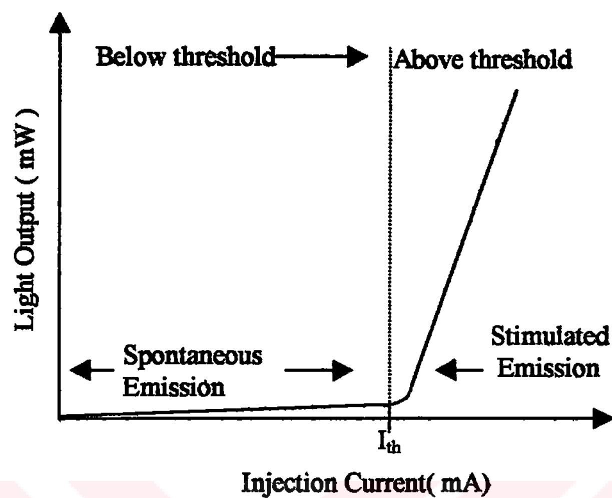

Figure 3.2 Light- Current (L - I) curve of a typical semiconductor laser.

CHAPTER 4

STRAINED QUANTUM WELL LASER STRUCTURES GROWN ON (111) GaAs

4.1 Introduction

The oldest, best developed and still most sophisticated heterostructure laser system is the AlGaAs-GaAs system. AlAs and GaAs have the same lattice constants. This allows the design of any structure, with any combination of layer compositions, without regard to lattice mismatch or the associated dislocation formation. The range of wavelengths available from lattice-matched AlGaAs-GaAs quantum well heterostructure laser is from $\lambda \approx 0.88$ - 0.65 μm. After AlGaAs-GaAs, the best studied semiconductor heterostructure laser materials system is InGaAsP-InP. High quality InP substrates are less readily available and more expensive so InGaAsP-InP quantum well heterostructure lasers are far less common. The range of wavelengths available from lattice-matched InGaAsP-InP quantum well heterostructure lasers is from $\lambda \approx 1.1$-1.6 μm. These wavelength ranges are sufficient to cover many important applications such as the use of modulated InGaAsP-InP lasers at $\lambda \approx 1.55$ μm as sources

for low loss, minimum dispersion optical fiber communication links, and the use of high power AlGaAs-GaAs laser arrays at $\lambda \approx 0.82$ μm for solid state lasers. But there is an obvious wavelength range of $\lambda \approx 0.88$-1.1 μm. This range is unavailable in any III-V lattice-matched heterostructure laser materials system. There are, however, a number of important applications that require laser emission in this range including frequency doubling of wavelengths near the 1.06 μm emission wavelength of Nd:YAG solid state lasers and pumping the upper states of rare-earth-doped silica fiber amplifiers.

An examination of the available direct gap III-V compound semiconductor alloys suggests that perhaps the best material system for obtaining emission wavelengths in the range $\lambda \approx 0.88$-1.1 μm is $In_xGa_{1-x}As$. There is, however, no suitable binary substrate material that allow lattice-matched composition of $In_xGa_{1-x}As$ in the wavelength range of interest. Thus, only a heterostructure materials system in which a very large mismatch must be accommodated (ε_0 as great as 3 %) may be considered.

Much of the current epitaxy focuses on the (001) substrate orientation because of wide range of growth conditions, which results in good epitaxial layer quality on this crystalline orientation. We study in this thesis the potential benefits of growing unstrained lasers, and strained using growth directions other than the conventional (001) direction. The highest valence band is highly anisotropic, even in unstrained bulk III-V semiconductors, where the heavy hole mass is approximately twice as large along (111) as along (111) [20]. This increases the number of heavy-hole confined states and the energy separation between the highest heavy and light hole states for a given well width. It has recently been shown that (111) GaAs-AlGaAs unstrained lasers can have lower threshold current density than equivalent (001) lasers [2,21]. Ghiti et. al. [22] described laser gain calculations, which shows that this improvement is consistent with the different valence subband structures associated with the two growth directions.

Tao and Wang [23] demonstrated for the first time a strained InGaAs QW laser grown on (111) GaAs at a wavelength of 988 nm with a threshold current density of 267 A/cm^2. Then Ishihara and Watanabe [24] succeeded in fabricating a strained

InGaAs quantum well laser on (111) GaAs with emission wavelength of 1072 nm and threshold current density of 164 A/cm^2. Smith and Mailhiot [6] predicted that due to lack of inversion symmetry in the zinc-blende structure, a net displacement of the positive and negative charges can be generated in a strained quantum well grown on a (111) substrate. As a result, if growth of strained zinc-blende semiconductors occurs away from the (001)-like directions, a large strain-induced internal electric field emerges via the piezoelectric effect [7]. The existence of this strain induced electric field across the well

i) Tilts the energy band structure modifying the carrier wave functions,

ii) Confines the electron and hole wave functions to opposite sides of the well leading to a decrease in the wave function overlap, and

iii) Pushes electron confined states to lower energies and the hole confined states to higher energies resulting in a decrease of the lowest transition energy.

These points have been illustrated in Fig. 4.1.

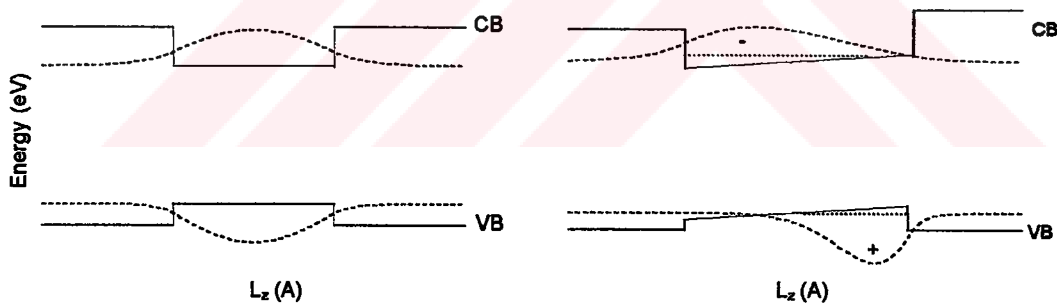

Figure 4.1 Conduction, valence band edges and carrier wavefunctions for quantum wells grown along (001) and (111) oriented substrates.

Furthermore, the built-in field can be compensated by applying an external field [8] or by photogenerated electron-hole pairs [25,26]. These pairs are spatially separated by piezoelectric field and forms two planes of opposite charge. This in turn induces an electric field that partially cancels (screens) the built-in field. The extend of

this screening will clearly depend on the density of electrons and holes. This carrier-dependent field effect has some potential application for nonlinear devices where the free carriers are generated by photo-absorption.

In addition, the critical thickness of strained In_xGa_{1-x} As layers grown on (111) GaAs is believed to be about twice that for (001) [5]. This enhancement of the critical layer thickness allows an increase of the In content in (111) strained In_xGa_{1-x} As quantum well lasers, which could in principle lead to emission at longer wavelengths on (111) substrates than that of (001) substrates.

4.2 Critical Thickness in Strained Layer Lasers

In lattice-matched heterostructure systems, the number and the thickness of quantum wells in the structure is not a design constraints. In a strained layer, lattice-mismatched system, however, the elastic accommodation of the strain energy associated with the mismatch, without the formation of misfit dislocations, must be considered [5,27]. Shown in Fig.4.2.a is a representation, at an exaggerated scale, of the unit cells of $In_xGa_{1-x}As$ and GaAs.

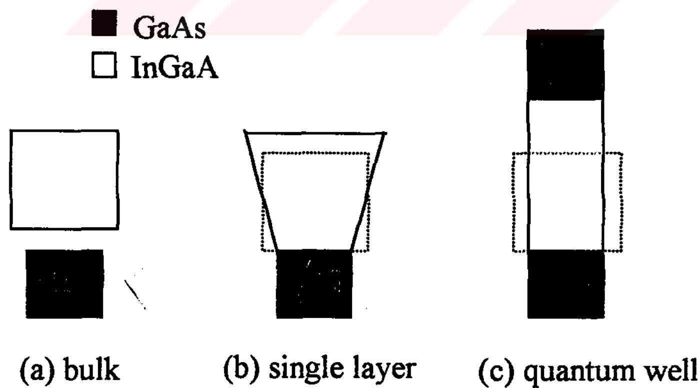

Figure 4.2 Schematic diagram (a) of separate $In_xGa_{1-x}As$ and GaAs unit cells, (b) a single strained layer $In_xGa_{1-x}As$ structure, and (c) an inserted $In_xGa_{1-x}As$-GaAs strained layer structure. Shown for reference, as a dashed line is the original $In_xGa_{1-x}As$ cell shape.

The unit cell of $In_xGa_{1-x}As$ can be as much as 3.6 % larger (x = 0.5) than GaAs, in contrast to $Al_xGa_{1-x}As$, which has a unit cell that is never more than about 0.13 % larger than the GaAs unit cell. In the case of single layer, as shown schematically assuming a relatively thick GaAs host in Fig.4.2.b, the $In_xGa_{1-x}As$ cell is shortened in both directions parallel to the interface (biaxial compression) and elongated in the direction normal to the interface (uniaxil tension). The strain energy that results is approximately equal to the misfit and produces a force F_e at the interface. If this force exceeds the tension F_l in a dislocation line, migration of a threading dislocation results in formation of a single misfit dislocations [5].

If the $In_xGa_{1-x}As$ cell is inserted between layers of the host as in a quantum well, assuming that the host is relatively thick on both top and bottom, both interfaces are under biaxial compression, as shown in Fig.4.2.c. The strain energy that results is again approximately equal to the misfit and, if the force F_e exceeds twice the tension F_l in a dislocation line, migration of a threading dislocation results in formation of two misfit dislocations [5]. In the case of a superlattice, where the concept of a host does not apply and alternating layers are under either biaxial compression or biaxial tension, the misfit strain is distributed among all of the layers, and the strain energy is equal to approximately half of the misfit.

For each of these cases, a critical layer thickness h_c, below which the misfit strain is accommodated without formation of misfit dislocations, can be defined in terms of elastic constants of the materials. Matthews and Blakeslee [5,28] calculate the critical thickness for layers in a superlattice having as equal elastic constants

$$h_c = \frac{a}{\kappa\sqrt{2}\pi\varepsilon_0}\frac{1-0.25\sigma}{1+\sigma}\ln(\frac{h_c\sqrt{2}}{a}+1), \qquad (4.1)$$

where h_c is the critical thickness, and a is the lattice constant of the strained layer. The misfit ε_0 is defined simply as

$$\varepsilon_0 = \frac{\Delta a}{a}, \tag{4.2}$$

and σ is Poisson's ratio, which is defined as

$$\sigma = \frac{C_{12}}{C_{11} + C_{12}}. \tag{4.3}$$

The coefficient κ has a value of 1 for a strained layer superlattice, 2 for a single quantum well, and 4 for a single strained layer. Fig.4.3 compares the critical thickness h_c of quantum well for (001) and (111) oriented growth. The calculated critical thickness on (111) is about two times larger than that on (001) over the entire Indium composition. This difference is mainly caused by the different θ value between (001) and (111) directions; i.e., $\cos\theta = 1/2$ for (001) and $\cos\theta = 1/2\sqrt{3}$ for (111). This means that the force acting to form the misfit dislocation is $\sqrt{3}$ times larger for (001), thus resulting in smaller critical thickness h_c.

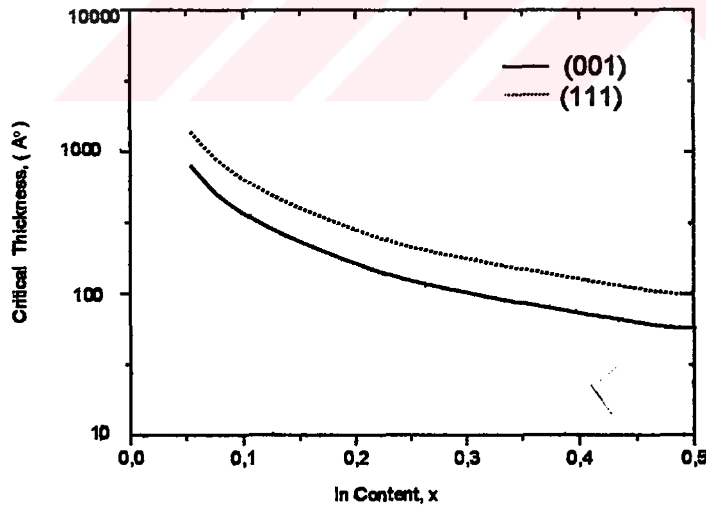

Figure 4.3 Comparison of the critical thickness of a strained quantum well grown on (111) and (001) oriented substrates calculated as a function of indium composition, using the Matthews and Blakeslee model.

T.C. YÜKSEKÖĞRETİM KURULU
DOKÜMANTASYON MERKEZİ

4.3 Orientation Dependence of Material Parameters

There are some fundamental differences in the orientation dependent material parameters between (111) and (001) bulk materials and between the quantum structures grown on these different oriented substrates. These difference will be presented in the next subsections.

4.3.1 Effective Masses

An important difference between quantum structures grown on (001) and (111) substrates is the different effective hole masses for these two orientations. The effective masses in the vicinity of the zone centre (k=0) are expressed in terms of Luttinger parameters (γ_1, γ_2 and γ_3) as follows

$$m^*_{hh,lh} = \frac{m_0}{\gamma_1 \mp 2\gamma_2} \text{ for (001),} \qquad (4.4)$$

$$m^*_{hh,lh} = \frac{m_0}{\gamma_1 \mp 2\gamma_3} \text{ for (111),} \qquad (4.5)$$

where m_0 is the free-electron mass, the upper sign stands for heavy-hole, and lower for light-hole. Lawaetz [29] calculated Luttinger parameters for all the III-V compounds. However, detailed experimental investigations [3,20,30,31] show the Lawaetz Luttinger parameters for GaAs lead to a much larger heavy effective mass than is observed along the (111) direction. So the Luttinger parameter set proposed by Molenkamp [20] is used for GaAs in our calculations. Resultant hole effective masses for GaAs and InAs are calculated and listed in Table 4.1. The material parameters for the ternary $In_xGa_{1-x}As$ are calculated by using the values of binary InAs and GaAs by interpolation technique. This technique is presented in Appendix A. The heavy- and light-hole effective masses for an increasing indium content are calculated by interpolation technique and are shown in Fig.4.4. It is seen from Fig.4.4 that the light-hole masses for both (001) and (111) orientation is more or less the same for the whole

range of indium composition. So that we can conclude that the light-hole effective masses has a weaker dependence on orientation. It is also seen from the same figure that the heavy-hole masses for the two orientation increases with increasing indium content.

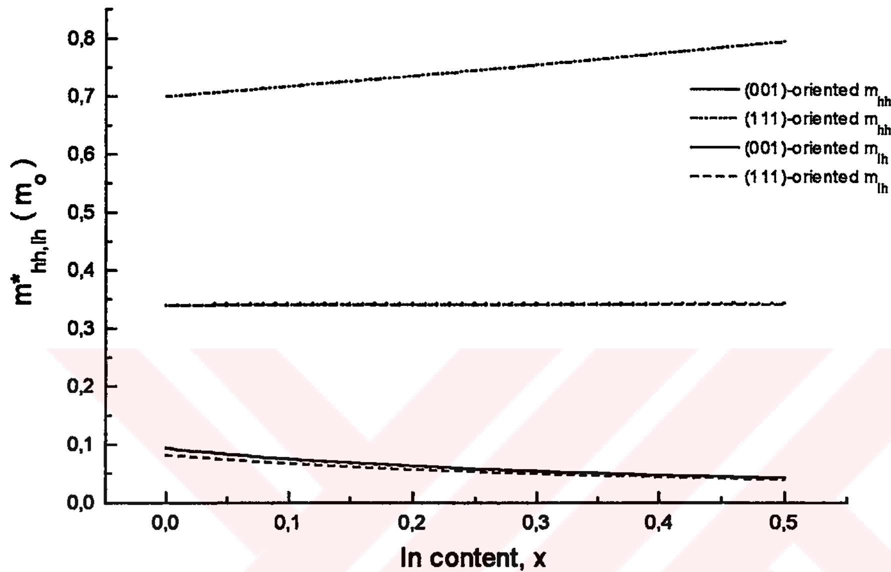

Figure 4.4 The heavy- hole and light-hole masses for both (001) and (111) orientation for the Indium content.

Table 4.1 Conduction-band edge effective mass $m_{\Gamma 6}$ and calculated hole effective masses for (001) and (111) orientations using Luttinger parameters from Molenkamp for GaAs and Lawaetz for InAs.

	γ_1	γ_2	γ_3	$m_{\Gamma 6}$	$m^*_{hh}(001)$	$m^*_{lh}(001)$	$m^*_{hh}(111)$	$m^*_{lh}(111)$
GaAs	6.790	1.924	2.681	0.067	0.339	0.094	0.7	0.082
InAs	19.67	8.37	9.29	0.023	0.341	0.027	0.917	0.026

However, the heavy-hole effective mass along the (111) direction is found to be about twice as that along (001). This causes the confinement energies of heavy-hole along

(111) direction being smaller than that of (001) orientation for the same well parameters.

4.3.2 Elastic Deformation and Strain-induced Band-edge Shift

For a sufficiently thin epilayer, all of the strain will be incorporated elastically in the layer. Consider the case of a compressively-strained layer. The epilayer is under a biaxial stress, such that its in-plane lattice constant $a_{\|}$ equals that of the substrate a_s.

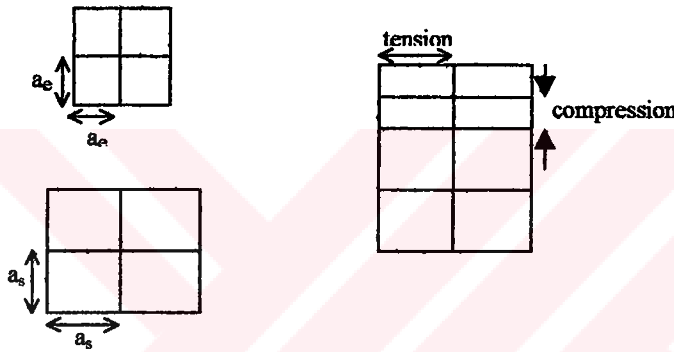

Figure 4.5 Illustration of the compression that results perpendicular to the growth direction for tension in the plane of the layers.

When the epilayer is grown on a (001) substrate, the perpendicular strain $\varepsilon_{\perp}$ is simply proportional to $\varepsilon_{\|}$, off-diagonal strain-tensor elements vanish, and the three major diagonal elements, ε_{ij} (i = x, y, z), can be expressed as

$$\varepsilon_{xx} = \varepsilon_{yy} = \frac{a_s - a_e}{a_e} = \varepsilon_{\|} \equiv \varepsilon_0 \tag{4.6}$$

$$\varepsilon_{zz} = -\frac{2C_{12}}{C_{11}}\varepsilon_0 = -\frac{2\sigma^{(001)}}{1-\sigma^{(001)}}\varepsilon_0, \tag{4.7}$$

where a_e and a_s are respectively the lattice constants of the epilayer and substrate material, C_{11} and C_{12} are the elastic stiffness constants, and ε_0 is the strain which,

increases with indium composition. The constant σ is known as Poisson's ratio, which is given as

$$\sigma=\frac{C_{11}}{2C_{12}}, \tag{4.8}$$

Since there is no stress in the growth direction it can be simply shown for a strained layer grown on an (001) substrate [32,33] that the different components of the strain tensor are given by

$$\begin{aligned} &\varepsilon_{xx}=\varepsilon_{\parallel}, \quad \varepsilon_{yy}=\varepsilon_{xx}, \quad \varepsilon_{zz}=\varepsilon_{\perp}. \\ &\varepsilon_{xy}=0, \quad \varepsilon_{yz}=0, \quad \varepsilon_{xz}=0. \end{aligned} \tag{4.9}$$

It is important to note that for (001) growth, the strain tensor is diagonal while for non-(001) directions, the strain tensor has nondiagonal terms.

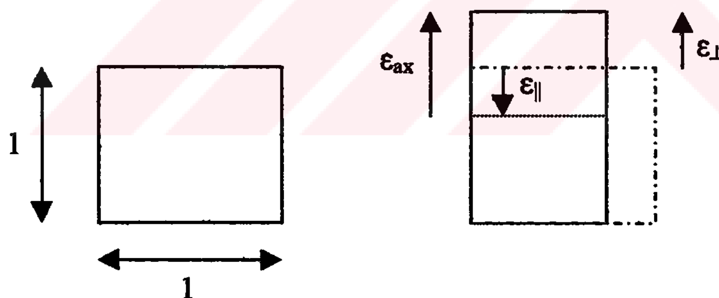

Figure 4.6 Illustration of strain decomposition for the case of biaxial compression in a cubic crystal. The unit cell on the left compresses in the plane (" || " direction) by a fractional amount, $\varepsilon_{\parallel}$, giving an increase in " height " $\varepsilon_{\perp}$. The axial strain, ε_{ax}, is the amount by which the crystal is extended in the " ⊥ " direction compered to the height it would have had (short dashed).

The total strain can be resolved into a purely axial component, ε_{ax}

$$\varepsilon_{ax} = \varepsilon_{zz} - \varepsilon_{xx} = -(\frac{C_{11} + 2C_{12}}{C_{11}})\varepsilon_0 , \tag{4.10}$$

and a hydrostatic component ε_{vol} $(= \frac{\Delta V}{V})$

$$\varepsilon_{vol} = \varepsilon_{xx} + \varepsilon_{yy} + \varepsilon_{zz} = 2(\frac{C_{11} - C_{12}}{C_{11}})\varepsilon_0 , \tag{4.11}$$

Therefore, there are two types of modifications that occur in the strained layer. The first effect is due to a change in the volume of the unit cell, known as the hydrostatic component, which gives rise to a change in the mean band gap ΔE_g by amount

$$\Delta E_g = (a_c - a_v) \varepsilon_{vol} \tag{4.12}$$

where a_c and a_v are the hydrostatic deformation potential of the conduction- and the valance-band, respectively.

The second, more important effect is due to the tetragonal deformation of the cubic crystal, which splits the degeneracy of the light and heavy-hole states at the valence-band maximum [34]. For small axial strain, the heavy and light-hole states are shifted by an energy $\pm$ S respectively, with respect to the mean valence-band edge energy. The magnitude of S, the strain-splitting energy, is dependent on the axial strain,

$$S = -b \, \varepsilon_{ax} \tag{4.13}$$

where b is the axial deformation potential. For compressive strain, the heavy hole levels are brought to the top of the valence band while tension strain brings the light-hole levels to the top of the valence band. A positive value of the S corresponds to biaxial compressive strain and a negative strain value of S to biaxial tensile strain.

For (111) growth, the tetragonal distortion is with respect to the (111) direction, not the cubic axes; consequently, the off-diagonal strain-tensor elements are nonzero in

this case. In the (111) oriented strained system, the strain tensor elements ε_{ii} and ε_{ij} are given by [35]

$$\varepsilon_{ii} = \frac{4C_{44}}{C_{11} + 2C_{12} + 4C_{44}} \varepsilon_{0,} \tag{4.14}$$

$$\varepsilon_{ij} = \frac{-(C_{11} + 2C_{12})}{C_{11} + 2C_{12} + 4C_{44}} \varepsilon_{0,} \tag{4.15}$$

where (i,j = x,y, z, i≠j). The band-edge shift for (111) quantum structures is related to the shear component of the deformation potential, d, due to the non-zero off-diagonal strain-tensor elements. Thus, the uniaxial and hydrostatic component of the strain are given as

$$S = \sqrt{3} d \varepsilon_{ij} \ , \tag{4.16}$$

$$\Delta E_g = 3 \ (a_c - a_v) \ \varepsilon_{ii} \tag{4.17}$$

4.3.3 Change in the Bandgaps and Emission Wavelengths for the two Orientations

The strain tensor elements for the (001) and (111) orientations are different. This results in a smaller Poisson ratio, given in Table 4.2, for (111) oriented growth, and consequently larger hydrostatic shifts compared to (001), yielding a strong orientation dependence to the energy difference between the conduction- and valence-bands. The hydrostatic and uniaxial strain corrections to the Γ point energy differences between the conduction- and valence bands for (001) and (111) are given respectively by,

$$\Delta E_{hh,lh} = -2a(\frac{C_{11} - C_{12}}{C_{11}})\varepsilon_0 \pm b(\frac{C_{11} + C_{12}}{C_{11}})\varepsilon_0, \tag{4.18}$$

$$\Delta E_{hh,lh} = -3a\varepsilon_{ii} \mp \sqrt{3}d\varepsilon_{ij} \tag{4.19}$$

where ΔE_{hh} and ΔE_{lh} are the shifts in the heavy-hole and light-hole valence-band edges with respect to the conduction-band edge. Table 4.2 gives the material parameters necessary to calculate Eqn. (4.16) and Eqn (4.17) for InGaAs strained layers on GaAs. The parameters for the ternary $In_xGa_{1-x}As$ quantum-well are constructed from a linear interpolation of the endpoint binary semiconductors, InAs and GaAs. The calculated variation in energy for the heavy- and light-hole valence band edges is shown in Fig.4.7.

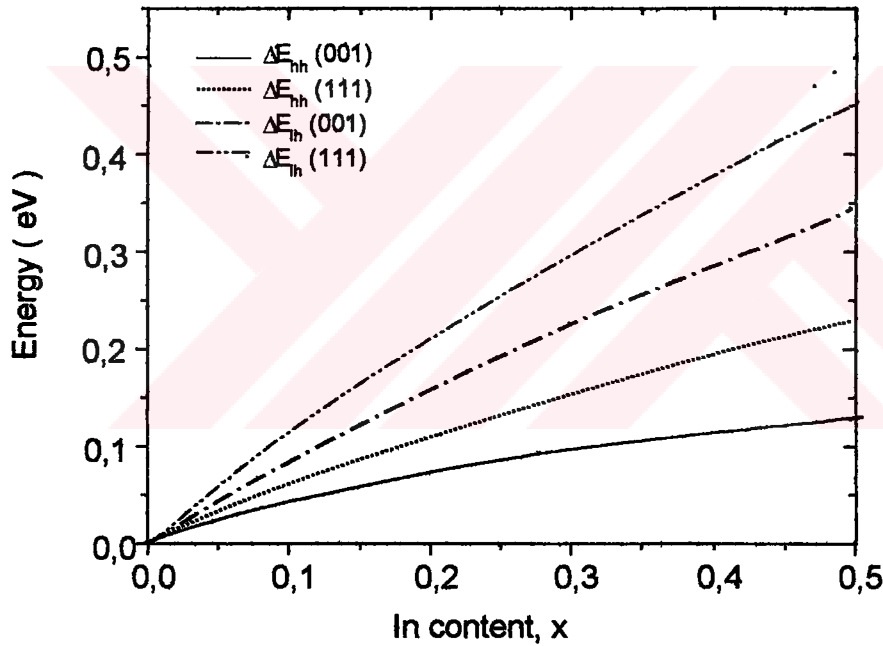

Figure 4.7 The shift in the heavy-hole valence band edge (ΔE_{hh}) and light hole valence band edge (ΔE_{lh}) with respect to the conduction band edge for (001) and (111) orientation as a function of In composition for $In_xGa_{1-x}As$-GaAs strained layers.

The shift of the heavy-hole and light-hole valence-band edge with composition is greater on (111) than on (001). This leads to a larger band gap on the (111) orientation

for a given composition. This enhancement of the band gap is mostly due to the hydrostatic pressure component of the strain. For tetrahedral semiconductors generally,

$$C_{11} \approx 2C_{12}, \qquad C_{12} \approx C_{44} \tag{4.20}$$

so that for (111) growth;

$$\varepsilon_{ii} \approx -\varepsilon_{ij} \approx \tfrac{1}{2}\,\varepsilon_0 \tag{4.21}$$

Therefore, a comparison of the hydrostatic pressure component of strain on (001) and (111) orientation shows that the hydrostatic pressure component of strain is 1.5 times larger on the (111) than (001) orientation.

Table 4.2 Semiconductor properties of GaAs and InAs used in the present calculation. All parameters are from Landölt – Bornstein (Vol.17a, 1982) unless otherwise noted, for a see reference [22].

	GaAs	InAs
a_0 (Å)	5.6533	6.0583
C_{11} (10^{11} dyne/cm^2)	11.81	8.33
C_{12} (10^{11} dyne/cm^2)	5.32	4.53
C_{44} (10^{11} dyne/cm^2)	5.94	3.96
a_c (eV)	-7.17[a]	-5.08[a]
a_v (eV)	1.16[a]	1.00[a]
b(eV)	-1.7	-1.8
d (eV)	-4.55	-3.6
e_{14} (C/m^2)	-0.16	-0.045
ε_r	12.91	15.15
$\sigma^{(001)}$	0.311	0.352
$\sigma^{(111)}$	0.186	0.222

The bulk bandgap energy of the $In_xGa_{1-x}As$ quantum well is calculated by using the Coleman's [36] expression of

$$E_g = 1.424 - 1.619\,x + 0.555\,x^2 \qquad (4.22)$$

and is shown in Fig.4.8 a.

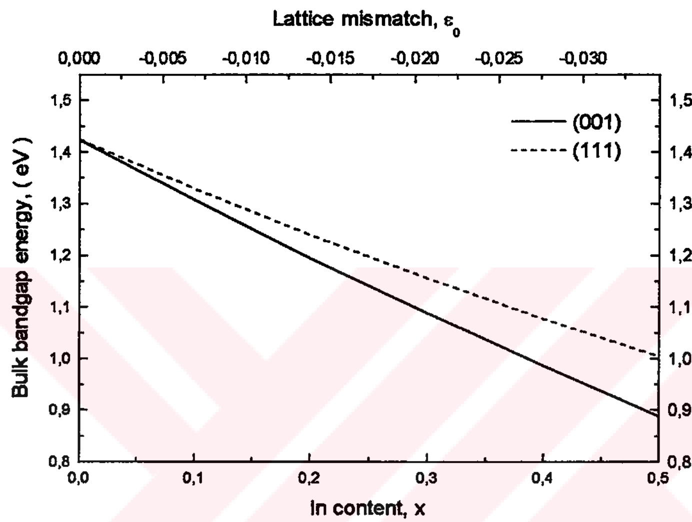

(a) Bulk Bandgap Energy

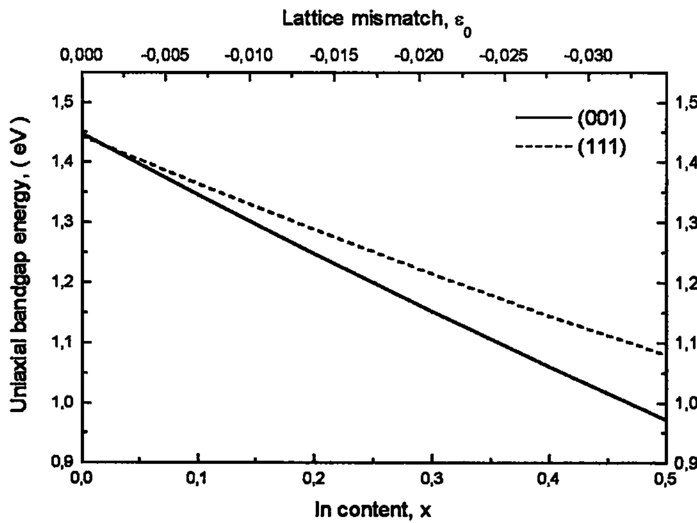

(b) Uniaxial Bandgap Energy

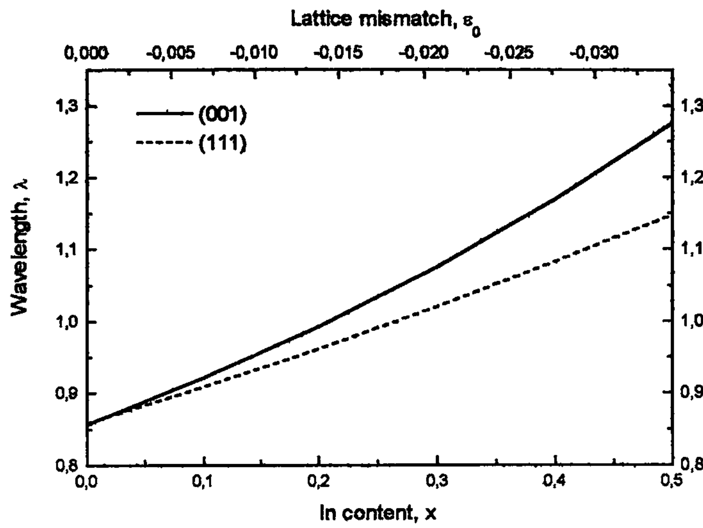

(c) Emission Wavelength

Figure 4.8 Schematic representation of the (a) bulk bandgap, (b) uniaxial bandgap energy, and (c) emission wavelength for $In_xGa_{1-x}As$ quantum well on (001) and (111) oriented GaAs substrates as a function of Indium composition.

It is seen that although the bulk bandgap energy decreases for the whole range of indium content for both (001) and (111) orientations, greater and much quicker reductions are obtained for (111) orientation. Similar trend is observed for uniaxial bandgaps for two orientations under investigation, see Fig.4.8.b. Such a reduction in energy bandgaps with increasing lattice mismatch results the emission wavelength to have longer and longer wavelengths for (001) growth for a fixed indium composition. This is illustrated in Fig.4.8.c. However, we should point out that we have not considered the effect of the confinement energies by calculating the emission wavelength in Fig.4.8.c. Because in quantum wells, the calculated electronic transition energies are increased further by the electron and heavy-hole quantum confinement energies, which depend directly upon quantum well thickness (L_z), and also upon indium content via the effective masses (m_e^*, m_{hh}^*, m_{lh}^*) and conduction-band and valence-band offsets.

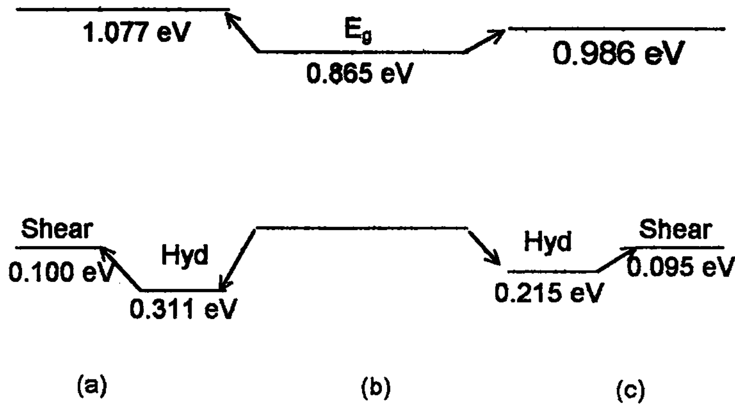

Figure 4.9 Schematic diagram of the band structure modification for both (a) (111) and (c) (001) orientations.

In Fig.4.9, band structure without strain effect is shown in the centre of figure. The energy change due to hydrostatic term is indicated by “hyd” and shear terms are shown successively. The hydrostatic term is larger for the (111) oriented structure than that of the (001) structure. From this figure, calculated band structure changes much larger in hydrostatic terms for the (111) than for the (001).

4.3.4 Piezoelectric Effect

A large internal electric field emerges in the strained layer region due to piezoelectric effect in the case of (111) oriented strained structures. The magnitude of the piezoelectric field is related to the off-diagonal components of strain tensor ε_{ij} by the following equation,

$$E_{Piezo} = \frac{2\sqrt{3}e_{14}\varepsilon_{ij}}{\varepsilon_0\varepsilon_r} \tag{4.23}$$

where ε_0 is the permitivity of free space, ε_r the dielectric constant of the material, and e_{14} is the piezoelectric constant.

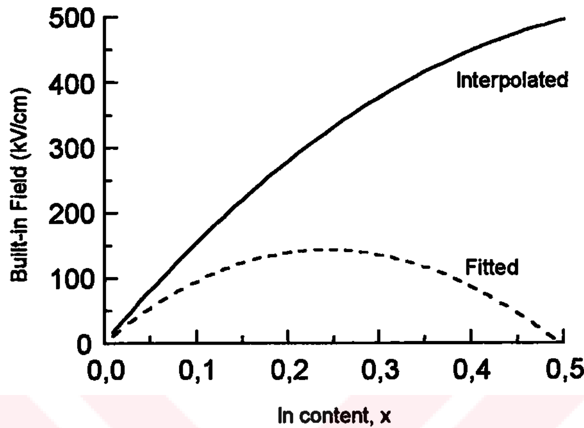

Figure 4.10 Calculated magnitude of the strain induced electric field versus In composition x in an elastically deformed $In_xGa_{1-x}As$ strained layer grown on (111) GaAs substrates by taking e_{14} as linear interpolation of standard values of binary compounds (solid line) and taking the fitted value of e_{14} (dashed line).

Moise et al [37] reported that their experimentally determined strain-induced electric field values agree well with theoretical calculations of Eqn.(4.23) using standard e_{14} values for In mole fractions in the range $0.037 < x < 0.09$. The calculated internal electric field for strained $In_xGa_{1-x}As$ on GaAs is shown in Fig.4.10 (solid line). The results were obtained by assuming a linear variation of the piezoelectric constant for $In_xGa_{1-x}As$ between InAs and GaAs. As can be seen from Fig.4.10 (solid line), the magnitude of the electric fields are very large, exceeding 10^7V/m, for lattice constant mismatches of the order of 1%. On the other hand, Fisher et al [38] reported a good agreement between theory and experiment only by using a value for the e_{14} constant 30% smaller than the commonly accepted value for an In content of 15%. Just recently, Sanchez et al [39] concluded from their work that the magnitude of E_{piezo} in

InGaAs alloys does not agree with a linear interpolation between the accepted values for InAs and GaAs. For the range of $0.07 < x < 0.23$ investigated, they have found $e_{14}(x)$ to be linear with x but significantly lower than that predicted by a simple linear interpolation of the accepted values for GaAs and InAs. Linear fitting to their experimental data gives

$$e_{14} = 0.115 - 0.2324x, \tag{4.24}$$

where x is the In mole fractions, and the units of e_{14} are C/m^2. The dashed line in Fig.4.10 shows the piezoelectric fields for InGaAs alloy calculated by using Eqn.(4.24). The built-in field increases to a maximum value when the indium composition is equal to 24%; then it starts to decrease with indium composition. The piezoelectric fields given by the dashed line of Fig. 4.10 show a completely different behaviour those obtained using standard values. Taking the standard values of e_{14} one deduces $E_{Piezo} = 450$kV/cm, (solid-line of Fig. 4.10), for strained $In_{0.4}Ga_{0.6}As$ quantum well. On the other hand, $E_{Piezo} = 87$ kV/cm when we take the fitting value of e_{14} (Eqn.4.24). The factor of 5 between this fit value and that determined from the interpolation of e_{14} using standard values emphasises the degree of uncertainty in our knowledge of piezoelectric constants.

As we see from the above discussion, the magnitude of the piezoelectric field remains unclear for the whole range of indium compositions of 0 - 0.50. On the other hand, it is obvious from the experimental investigations [37,38,39] that the experimental strain-induced electric field values do not agree with theoretical calculated linear interpolation for indium compositions $x > 0.1$. To the best of our knowledge, an experimental study of the magnitude of the piezoelectric field $x \sim 0.40$ has not yet been undertaken. Therefore, we have chosen the fitted value of Sanchez et. al. [39] to predict the magnitude of the strain-induced piezoelectric field for strained $In_{0.4}Ga_{0.6}As/GaAs$ laser structure.

4.4 Energy Levels and Wavefunctions

The effect of the growth orientation of quantum well lasers is calculated taking into account orientation dependent material parameters such as effective mass, elastic deformation, and strain-induced band edge shifts. The quantized energy levels and their corresponding wavefunctions for the carriers in the conduction and valence band are determined numerically by solving Schrödinger's equation of

$$-\frac{\hbar^2}{2m^*}\frac{d^2\psi(z)}{dz^2}+[V_r(z)+V_F(z)]\psi(z)=E\psi(z), \tag{4.25}$$

for a quantum well of width L_z using the finite difference method [40]. ψ is the carrier envelope wavefunction, m^* is the carrier effective mass, $V_r(z)$ is the potential due to the quantum well, and $V_F(z)$ is the tilted potential due to the strain-induced built-in piezoelectric field for non-(001) oriented materials which is given by

$$V_F(z)=\pm eF\,z. \tag{4.26}$$

$V_F(z)$ is set to zero for (001) orientation.

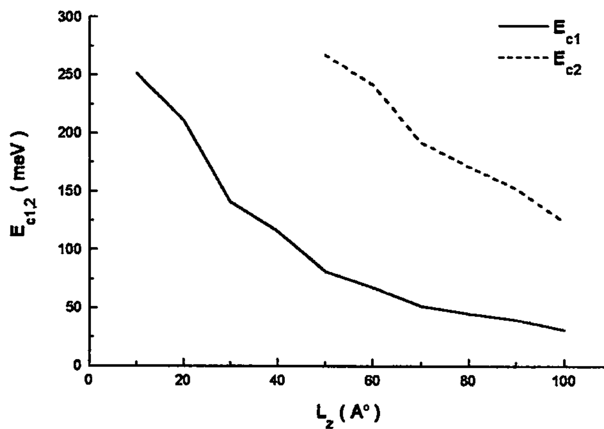

Figure 4.11. Calculated quantized energy levels for the electrons for (001) growth.

Figure 4.11 shows the calculated energy levels for electrons for (001) growth. It is seen from Fig.4.11 that when the barrier thickness is constant and only the well thickness altered, the confined energies get closer to the bottom of the well i.e. they get smaller, as the well width becomes thicker. This is true for both electrons and holes in each orientations of (001) and (111). In addition, the number of confined states increases with increasing well width, as can be seen from Fig.4.11.

The wavefunction is known to be sinusoidal oscillations in the well and decay exponentially in the barrier layer. This method is applicable to both (111) and (001) quantum wells. Fig.4.12.a and Fig.4.12.b, compares the confined heavy- and light-hole states for (001) and (111) orientation

As can be seen from the figures there are more confined hole states on (111) orientation for a fixed well width due to the increase in the perpendicular hole mass as we have mentioned in section 4.3.1. The presence of more energy levels brings a disadvantage because one has to inject more and more carriers to achieve population inversion and this in turn increases the threshold current density which we do not want.

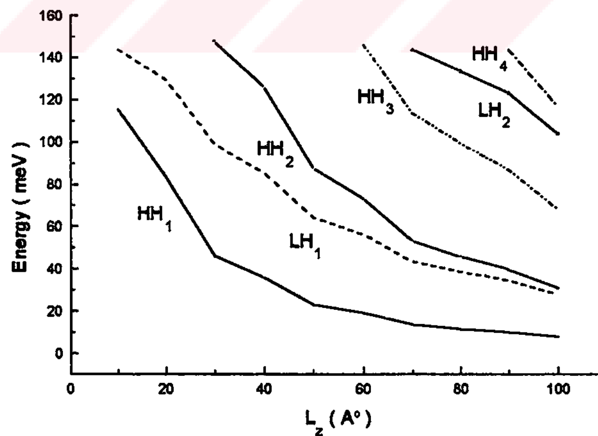

(a) (001) oriented

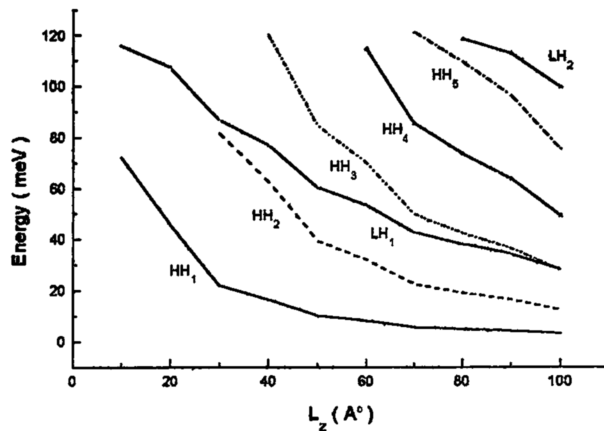

(b) (111) oriented

Figure 4.12 The confined heavy- and light-hole states for (001) and (111) orientation as a function of well width.

The presence of the internal piezoelectric field perturbs the quantum well potential energy profile from that of a symmetric finite square well to that of a highly asymmetric well (see Fig.4.1) with a corresponding finite tunnel barrier and the electron and hole wavefunctions are pinned against opposite to the quantum well heterointerfaces. This effect is illustrated in Fig.4.13a, b, c, and d. As can be seen from Fig.4.13, the wavefunction of the first confined electron state is pushed to left and the wavefunction of the first confined heavy-hole state is pushed to the right of the quantum well gradually when the field increases from 0 to 120 kV/cm. As a consequence of this the oscillator strength for the n=1 electron to heavy-hole (e-hh) exciton is decreased significantly compared to the zero electric field case (flat-band case).

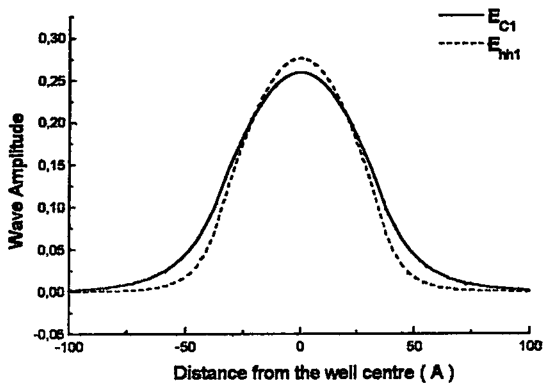

(a) No Applied field

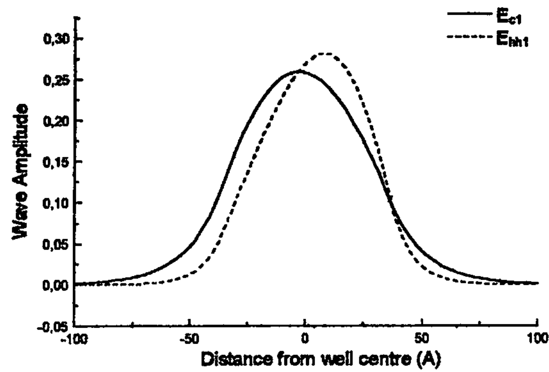

(b) F = 40 kV/cm

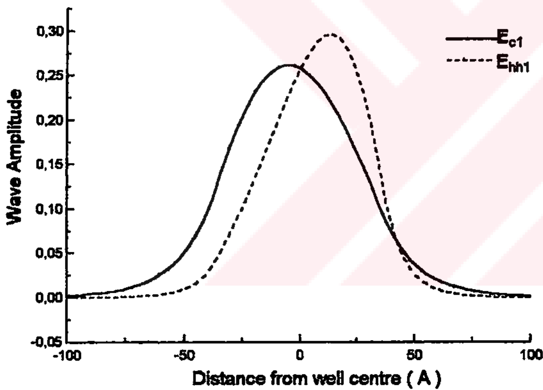

(c) F = 80 kV/cm

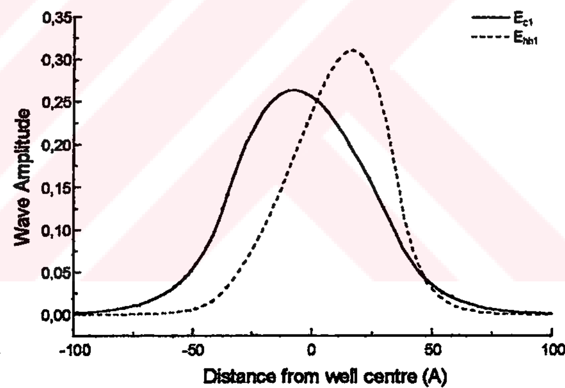

(d) F = 120 kV/cm

Figure 4.13 Wavefunctions for the first confined electron state in conduction band and the first confined heavy-hole state in valence band in a quantum well in the presence of an internal piezoelectric field.

As a consequence of the movement of the electron wavefunctions to one end and the hole wavefunctions to the other end, due to the piezoelectric field, the transition

energy is lowered relative to the zero electric field case. This can be seen from a closer examination of Fig.4.14a for a fixed value of the well depth.

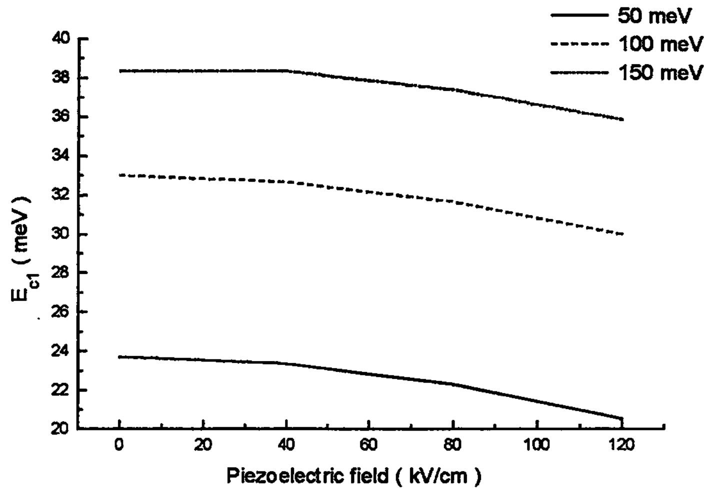

(a)

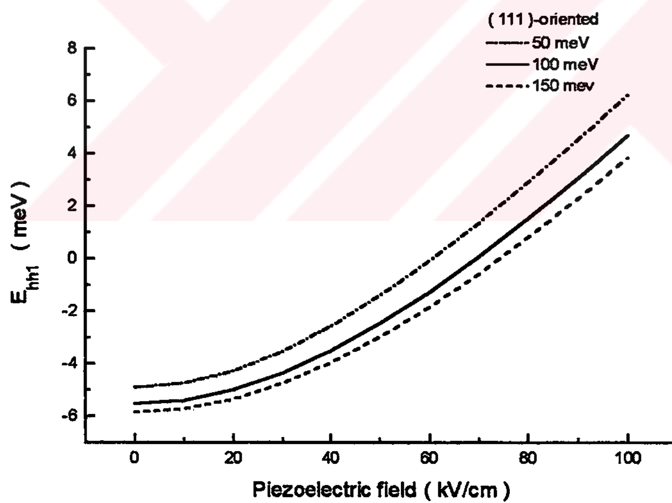

(b)

Figure 4.14 The confinement energies of both first electron- and hole-states as a function of piezoelectric field for different band-offsets (well-depths).

The comparison of the variation of the confinement energy of the electron and hole in Fig.4.14a and b for a fixed band-off-set value reveals that the energies of the

heavy-holes shift as a function of the electric field faster than that of the electron level. The larger energy shift from the heavy-hole compared to the electron level can be attributed to the larger heavy-hole effective mass.

It is seen that the E_{c1} values decreases with increasing internal piezoelectric field for a fixed ΔE_c, i.e. E_{c1} values gets closer to the bottom of the well. A similar variation is obtained for the first heavy-hole state, and again it is seen that the E_{hh1} gets closer to the bottom of the well for a fixed valence-band-offset value, ΔE_v. This illustrates that the transition energy of the (e1-hh1) exciton is lowered with increasing internal field.

It can be concluded from Fig.4.14.a and Fig.4.14.b that the increase in the magnitude of the band-offsets increases the confinement energies of both electron- and hole-states. The increasing magnitude of the band-offsets also causes the amplitude of the wavefunctions to get bigger. This is shown in Fig.4.15 for the first heavy-hole state as a function of an internal piezoelectric fields for different values of valence band-offsets. The band offset determines the depth of the corresponding well.

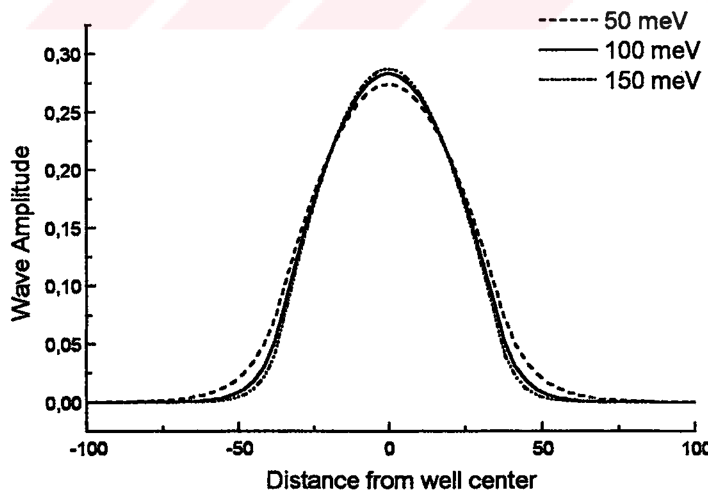

(a) No Applied Field

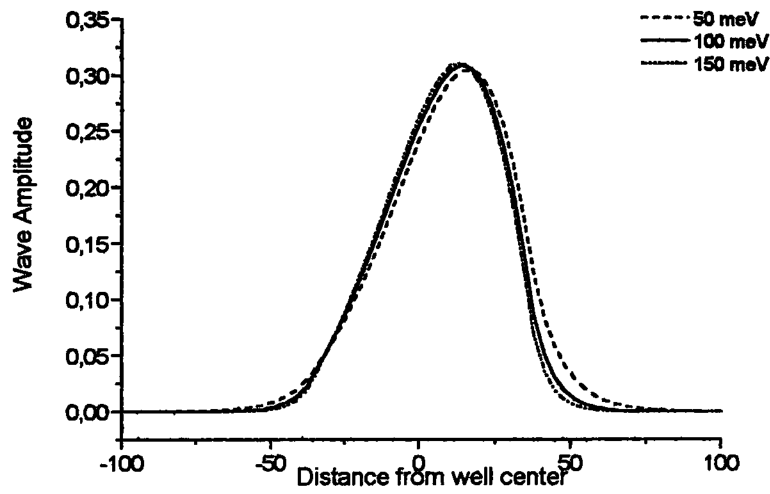

(b) F = 40 kV/cm

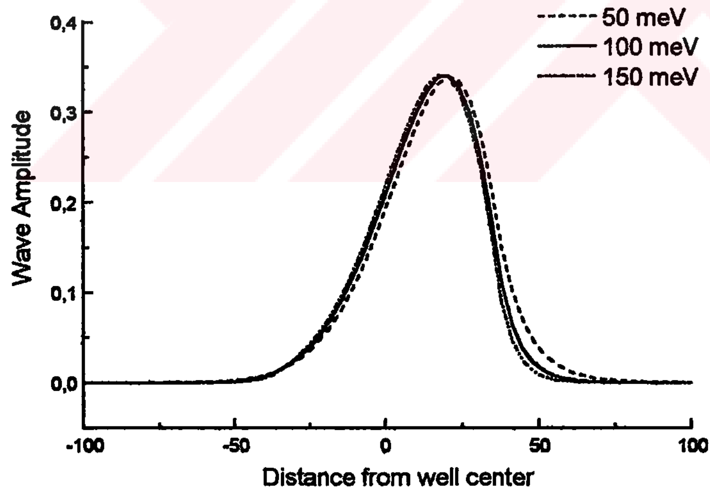

(c) F = 80 kV/cm

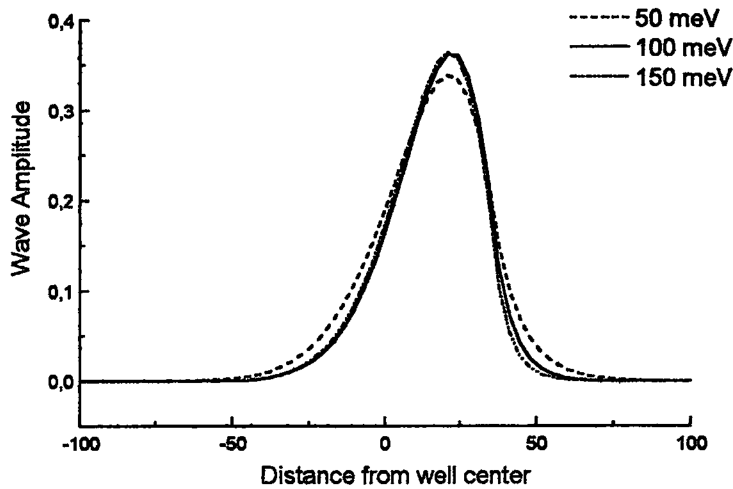

(d) F = 120 kV/cm

Figure 4.15 The amplitude of the confined energy level of first heavy-hole state, E_{hh1}, with increasing piezoelectric field for three different values of valence-band-offset, ΔE_v .

We have shown that, when there is a significant piezoelectric field across the (In, Ga) As layers, then the e1-hh1 exciton in the (111) orientation should be at a lower energy than in their (001) counter parts. The difference between the (001) and (111) orientation is the greatest for the widest well width, see Fig.4.16.

As can be seen from Fig.4.16 the shift in the confinement energy of the first heavy-hole state is the greatest for the largest field. A similar variation is obtained for the electron state. So, these changes to the n=1 e-hh exciton transition are expected to be more dramatic for a wide quantum well than for a narrow well because the spatial separation between the centroids of the electron and hole wavefunctions is greater, and the quantum confinement energies are closer to the perturbation at the bottom of the well.

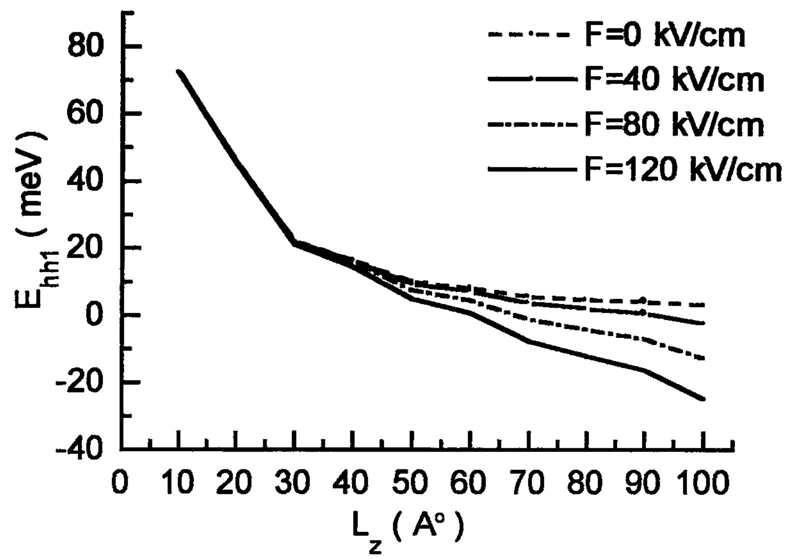

Figure 4.16. The shift in the confinement energies of the first heavy-hole state.

CHAPTER 5

GAIN IN QUANTUM WELL LASERS

5.1 Introduction

The application of quantum well structures to semiconductor lasers has received considerable attention because of physical interest as well as superior characteristics, such as low threshold current [41], an increase in differential gain, lasing tunability, and excellent dynamic properties [42]. The optical gain is a key parameter in quantum well lasers [43,44].

In this chapter, the theory of the laser gain in quantum well structures has been reviewed taking into account the effects of the intraband relaxation to compare the gain characteristics of the (001)- and (111)-oriented quantum well lasers.

5.2 Gain Theory

The main factors determining an optical spectrum are the carrier distribution in the energy band, the transition matrix elements between the electrons and holes, and the intraband relaxation of carriers due to various scattering process. The carrier distribution determines the overall profile of the spectrum and the relation

between the peak intensity and carrier density. The change in the density of states as going from 3D to 2D brings about various superior characteristics, such as an increase in differential gain and reduction in threshold current density [45,46]. Built-in strain can also further reduce the carrier density at threshold.

The transition matrix element determines the intensity of the gain spectrum along a given polarisation direction because the gain in a semiconductor laser is proportional to the absolute square of the dipole moment R_{cv} along the electric field direction [47]. The dipole moments can be related to the momentum matrix elements M_{cv} by k.p theory as

$$M_{cv} = \frac{m_o E_{cv}}{i\hbar e} R_{cv} \tag{5.1}$$

The anisotropy of the transition matrix element leads to the polarization dependence of quantum well laser gain spectrum [43,48,49]. This can be explained as follows [50]; the important optical transitions in a laser are associated with electrons in the s-like conduction band recombining directly with holes in the predominantly p-like valence bands. The photon emitted in this process can have polarisation components along the x, y, and z axes of the laser, in which we choose the axis of quantisation along the growth direction z, with x along the axis of the laser cavity as shown in Fig. 5.1.

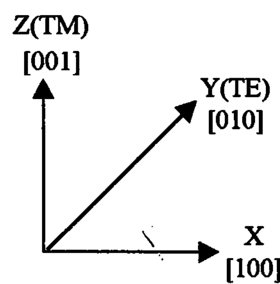

Figure 5.1 The coordinate system.

TM gain is due to the electrons recombining with holes in z-like states to give light polarised along the z direction and TE gain to electrons recombining with y-like valence states. The valence bands have equal contributions from x-, y- and z-like states, so that spontaneous emission has equal components polarised along the

three principal axes. Hence, when carriers are injected into such a laser, equal proportions can contribute to TE gain, TM gain and to unwanted spontaneous emission (x-like) polarised along the direction of the laser cavity.

In compressive strain the heavy-hole state shifts upwards in energy, Fig.2.6. As this state has no z-character and equal x and y-character, TE gain will be enhanced and TM gain suppressed. Approximately one in two carriers near the band edge will contribute directly to overcoming relevant losses, so that the threshold current density should decrease and the TE differential gain should increase compared to that of the unstrained case. In tensile strain the light-hole state shifts upwards in energy, Fig.2.6. This state has approximately two-thirds z-like character for small strain energy S, and thus TM gain is enhanced. The situation in tensile strain is then even better than in compressive strain.

Intraband relaxation causes a broadening of the optical spectrum, leading to a reduction in the peak values of the gain and emission spectra [51,52]. This effect is more remarked in quantum well lasers [43,53], with the gain spectra becoming smooth and broad in spite of the sharp step-like density of states.

i. Quantized Energy Levels and Carrier Densities

The schematic energy band diagram for a typical quantum well structure is shown in Fig. 5.2. The transition energy E_{cv} and corresponding angular frequency ω are written by

$$E_{cv} = \hbar\omega = E_{cjk_\parallel} - E_{vj'k_\parallel} \tag{5.2}$$

with $E_{cjk_\parallel}$ and $E_{vj'k_\parallel}$ assuming parabolic bands as

$$E_{cjk_\parallel} = E_{cj} + \frac{\hbar^2 k_\parallel^{\,2}}{2m_c}, \tag{5.3}$$

$$E_{vj'k_\parallel} = -E_{vj'} - \frac{\hbar^2 k'^{\,2}_\parallel}{2m_v}, \tag{5.4}$$

with the quantized energy levels E_{cj} and $E_{vj'}$ of the quantum well and effective masses m_c* and m_v*. In the subscripts $cjk_{\|}$ and $vj'k_{\|}$, c and v refer to the conduction and valence bands, respectively, j and j' are the subband numbers of a quantum well structure, and $k_{\|}$ and $k_{\|}'$ are the wave vectors parallel to the well interface.

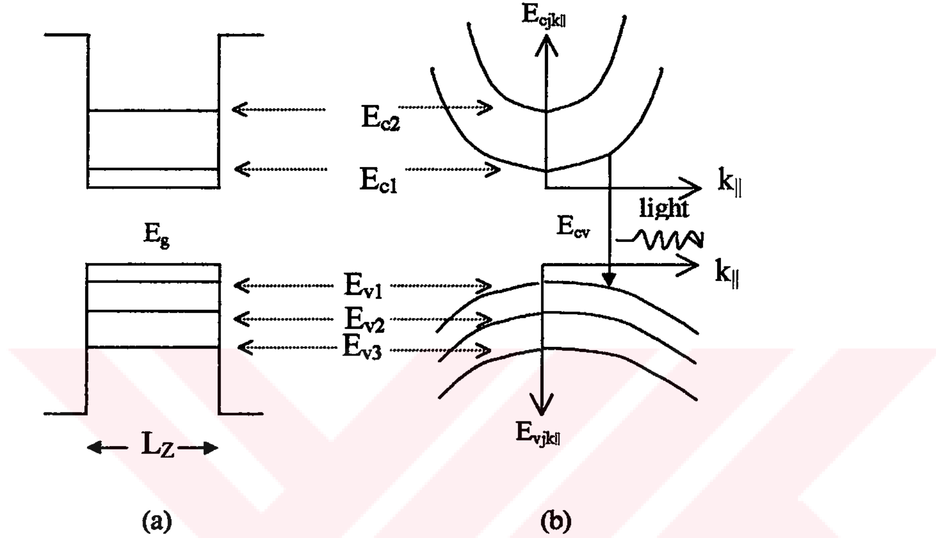

Figure 5.2 Conduction and valence (a) wells and quantized energy levels, and (b) subband structures and optical transition.

For momentum-conserving transitions, the photon wavevector is negligible by comparison with the carriers, and so we have

$$k_{\|} = k_{\|}', \quad \text{(k – selection rule)} \tag{5.5}$$

so that the transition energy E_{cv} can then be written as

$$E_{cv} = E_g + E_{cjk_{\|}} + E_{vj'k_{\|}}, \tag{5.6}$$

$$E_{cv} = E'_g + \frac{\hbar^2 k_{\|}^2}{2m_c^*} + \frac{\hbar^2 k_{\|}^2}{2m_v^*}. \tag{5.7}$$

The primed energy gap, $E'_g = E_g + E_{cj} + E_{vj'}$, is defined as the bandgap between two given subbands in a quantum well and E_g is the band gap energy of the material. The individual energies $E_{cjk_{\|}}$ and $E_{vj'k_{\|}}$ are related to the transition energy E_{cv} by

$$E_{cjk_{\parallel}} = E_{cj} + \frac{m_r}{m_c}\left[E_{cv} - (E_g + E_{cj} + E_{vj'})\right] \tag{5.8}$$

while the energy of the electron in the valence band

$$E_{vj'k_{\parallel}} = -E_{vj'} - \frac{m_r}{m_v}\left[E_{cv} - (E_g + E_{cj} + E_{vj'})\right] \tag{5.9}$$

where

$$\frac{1}{m_r} = \frac{1}{m_c} + \frac{1}{m_v}. \tag{5.10}$$

Positions of these energy levels are schematically shown in Fig.5.2. It is important to note that each subband transition will have its own band gap energy E'_g.

The carrier density in a given band can be found for a given quasi-Fermi level by integrating the density of states multiplied by the occupation probability over the entire band;

$$n = \int_{E_{cj}}^{\infty} \rho_c(E_{cjk_{\parallel}}) f_c(E_{cjk_{\parallel}}) dE_c, \tag{5.11}$$

$$p = \int_{-\infty}^{E_{vj'}} \rho_c(E_{vj'k_{\parallel}})(1 - f_v(E_{vj'k_{\parallel}})) dE_v. \tag{5.12}$$

and the f_c and f_v are the Fermi distribution functions of the electron in the conduction band and in the valence band,

$$f_c = \frac{1}{[(\exp(E_{cjk_{\parallel}} - E_{fc})/k_b T) + 1]}, \tag{5.13}$$

and

$$f_v = \frac{1}{[(\exp(E_{vj'k_{\parallel}} - E_{fv})/k_b T) + 1]}, \tag{5.14}$$

where E_{fc} and E_{fv} are the quasi-Fermi level for conduction and valence band, respectively. For parabolic QW subbands, such as we are considering here, the electron concentration can be obtained by substituting density of states equation of

$$\rho_{QW}(E) = \frac{m^*}{\pi \hbar^2 L_z} \tag{5.15}$$

and Eqn.(5.13) into Eqn.(5.11) as

$$n = \frac{m_c^* k_B T}{\pi \hbar^2 L_z} \sum_j \ln\left[1 + \exp(-(E_{cj} - E_{fc})/k_B T)\right] \tag{5.16}$$

The sum here is over all quantized subbands within the conduction band of the quantum well and E_{cj} are the quantized energy levels. The effective mass m_c^* refers to the in-plane effective mass of electron. A corresponding formula exists for holes.

ii. Linear Gain

The linear gain $\alpha(\omega)$ calculations for quantum wells have been carried out the theory developed by Asada [54] who used the density-matrix theory with relaxation broadening [51,55]. The linear gain $\alpha(\omega)$ is then given for parabolic bands by the following equation of

$$\alpha(\omega) = \omega \sqrt{\frac{\mu}{\varepsilon}} \frac{m_c^* m_v^*}{(m_c^* + m_v^*)} \frac{1}{\pi \hbar^2 L_z} \sum_{j,j'} \int_{Eg+E_{cj}+E_{vj'}}^{\infty} < R_{cv}(E_{cv})^2 >$$

$$* (f_c(E_{cjk_\parallel}) - f_v(E_{cj'k_\parallel})) \frac{(\hbar/\tau_{in})}{(E_{cv} - \hbar\omega)^2 + (\hbar/\tau_{in})^2} dE_{cv} \tag{5.17}$$

with a Lorentzian broadening function

$$L(\hbar\omega) = \frac{\hbar/\tau_{in}}{(E_{cv} - \hbar\omega)^2 + (\hbar/(\tau_{in}))^2}, \tag{5.18}$$

where τ_{in} is the intraband relaxation time that characterise the decay time of the dipole formed by the recombining electron and hole, which interacts with the electromagnetic wave. E_{cv} is the transiton energy, ω is the angular frequency of

light, μ is the free space permeability, ε is the dielectric constant, $m_c^* m_v^*/(m_c^*+m_v^*)$ is the reduced mass, and L_z is the well width. $<R_{cv}(E_{cv})^2>$ is the averaged square of the dipole moment. The dipole moment $<R_{cv}^2>$ for one subband averaged over all possible directions in a quantum-well structure is expressed in terms of that in a bulk laser $<R_{cv}^2>_{bulk}$ and given as a function of the energy of the electron above the band-edge for the heavy-hole transition as [49,54]

$$< R_{cv}^2 > \approx \frac{3}{4}\langle F_v | F_c \rangle^2 \delta_{k_{c\parallel}k_{v\parallel}} (1 + \frac{E_{cj}}{E_{cjk_\parallel}}) \langle R_{cv}^2 \rangle_{bulk} \tag{5.19}$$

where

$$\langle R_{cv}^2 \rangle_{bulk} \approx \frac{2}{3} (\frac{e\hbar}{2E_{cv}})^2 \frac{2|M|^2}{m_0^2}, \tag{5.20}$$

for TE modes. $|M|^2$ is the transition matrix element and $<F_c|F_v>$ is the conduction and valence zone-centre envelope functions overlap. The most accurate estimates of the square of the momentum matrix element are reported by Corzine et al [56] for several material systems which are commonly used in semiconductor laser applications.

The linear gain coefficient in Eqn.(5.17) includes the factor f_c Eqn.(5.13) and f_v Eqn.(5.14), the difference $(f_c - f_v)$ which is the population difference between the conduction and valance bands. The probability of the downward transition of electron from a level in the conduction band to a level in the valance band is limited by the Pauli's exclusion principle, being proportional to electron density in the upper level multiplied by the hole density in the lower level, which is proportional to $f_v(1 - f_c)$. In these two transitions, the former gives light emission, while the later gives light absorption. Therefore, the net emission probability, i.e. the emission probability minus the absorption probability, is proportional to

$$f_c(1 - f_v) - f_v(1 - f_c) = f_c - f_v . \tag{5.21}$$

This is the origin of the factor $(f_c - f_v)$ in the Eqn (5.17).

Another important parameter is the quasi-Fermi levels and the carrier density in Eqn.(5.17). These parameters are determined by using the condition for charge neutrality which requires that n = p (for an undoped quantum well) and puts a

relation between E_{fc} and E_{fv}. From Eqn.(5.17), when $E_{fc} - E_{fv} > \hbar\omega$, $\alpha(\omega)$ is positive and an incoming light wave with photon energy $\hbar\omega$ will be amplified. We therefore require that, quasi-Fermi level separation must be greater than the bandgap to achieve optical gain in the material, i.e.,

$$E_g < \hbar\omega < E_{fc} - E_{fv}. \tag{5.22}$$

When the quasi-Fermi level separation is equal to bandgap, $E_{fc} - E_{fv} = E_g$, the material will become transparent for photon energies equal to the bandgap, according to Eqn.(5.22). Under equilibrium condition, $E_{fc} = E_{fv}$, and optical gain is impossible to achieve. The electron and hole carrier density that is required to provide this separation is known as the transparency carrier density, n_{tr} and its magnitude is related to the densities of states ρ_c and ρ_v of a given material. Optical gain is attained when the carrier density exceeds n_{tr}, such that the quasi-Fermi levels are separated by an energy greater than the bandgap.

5.3 Linear Gain in (111) Oriented Strained Quantum Well Lasers

Gönül [57] has examined the change of the maximum gain with piezoelectric field in (111) oriented strained InGaAs quantum well lasers assuming an intra-band relaxation time of $\tau_{in} = 10^{-13}$ s which corresponds to a level broadening of 6.7 meV. The polarization is assumed to be TE and the temperature is 293 K. Gönül has shown that the peak gain decreases in the presence of an internal piezoelectric field. We comment here on the implications of this earlier result. As an example, she has chosen the $In_{0.4}Ga_{0.6}As$ / GaAs quantum well laser structure of Ishihara et al [24]. The electric field is generated by the piezoelectric effect inside the quantum well due to the polarization charges that occurred at the interface between barrier and the quantum well. The existence of the strain-induced internal field across the well tilts the energy band structure and confines the electron and heavy-hole wavefunctions to opposite sides of the quantum well, leading to a decrease in the wavefunction overlap. It also pushes electron confined states to lower energies and the hole confined states to higher energies resulting in a decrease of transition

energy. Furthermore, the asymmetric potential-energy profile of the (111) oriented QW yields an increase in the strength of the transitions which are "forbidden" in the symmetric square well case. This is simply because the electron and hole wavefunctions are no longer sinusoidal and all the overlap integrals are in general non-zero. Thus, all the "forbidden" and "allowed" transitions having non-zero overlap integrals contribute to the gain. So, all transitions having nonzero overlap integrals was taken into account for gain calculations on (111) oriented lasers.

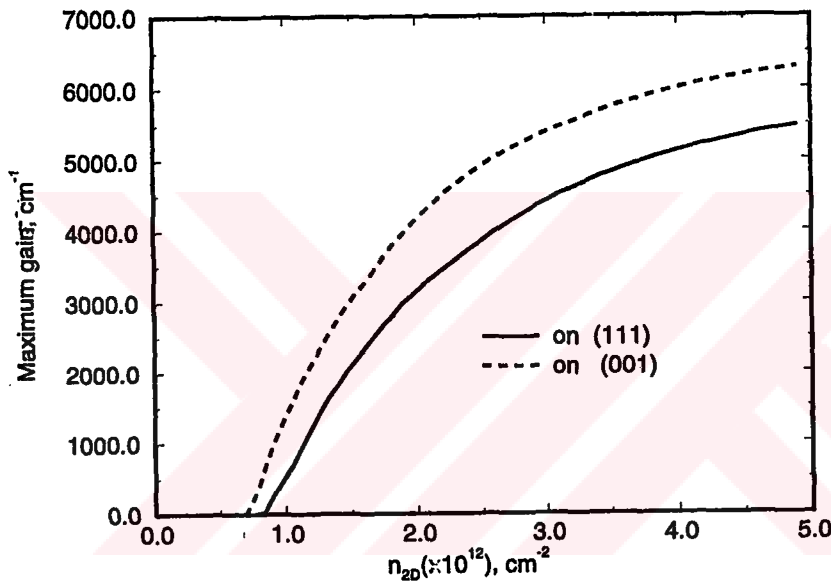

Figure 5.3 Calculated maximum gain versus injected carrier density for 0, 50, 100 and 150 kV/cm internal fields in 70 Å $In_{0.4}Ga_{0.6}As$ quantum well laser on a (111) GaAs substrate.

Although all transitions having non-zero overlap integrals contribute to the gain, the decrease in the strength of the symmetry allowed HH1-C1 transition due to the piezoelectric field yields a smaller maximum gain compared to the zero field case. Fig.5.3 shows the maximum gain versus carrier density at fields of 0, 50, 100 and 150 kV/cm including all transitions having non-zero overlap integrals [57].

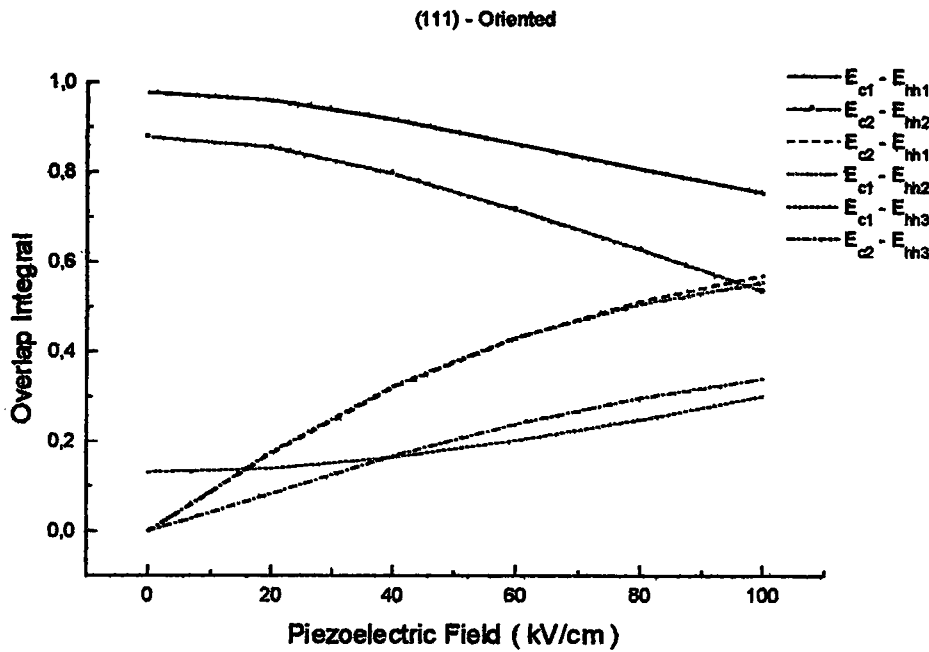

Figure 5.4 Calculated overlap integrals as a function of piezoelectric fields for all allowed and forbidden transitions.

Firstly, the transparency carrier density shifts slightly to lower carrier density with increasing piezoelectric field due to the increased HH1-HH2 separation in compressively strained lasers. The fundamental transition energy between the lowest electron state and highest heavy hole state which defines the point of transparency of the device (i.e. the lowest energy photons that can be absorbed) also reduces with increasing piezoelectric field shifting the lasing energy at the transparency carrier density. Secondly, the existence of the strain-induced piezoelectric field decreases the C1-HH1 overlap integral and lowers the peak gain curve, causing the threshold carrier density to shift to higher carrier densities. Therefore, the presence of a piezoelectric field lowers the transparency carrier density but increases the threshold carrier density.

As mentioned before, the peak gain decreases with an increase in the internal field through the quantum well. We try to explain this behaviour by means of the variations of the overlap integrals for allowed and forbidden transitions with internal piezoelectric field. Fig.5.4 shows how the strength of the overlap integrals

for all confined states vary with internal field. As can be seen from Fig.5.4 the strength of the overlap integrals of allowed transitions decreases with increasing field whereas it increases for forbidden transitions. C1-HH1 transition gives the most important contribution to the gain at lower carrier densities because only the first electron and heavy-hole band are significantly populated by the injected electrons and holes at these carrier densities. The oscillator strength of the C1-HH1 transitions becomes smaller with increasing piezoelectric field (see solid line in Fig.5.4). This is the reason why the presence of piezoelectric fields lowers the peak gain curve.

When carrier injection via the p-n junction starts, electron-hole pairs are created to screen out the effect of the strain-induced field on the band structure. As the electron-hole pairs screen out the field, the bands flatten out and the confined state energies move to higher values. So the relative strength of the symmetry "allowed" transitions increase. On the other hand, the relative strength of the "forbidden" transitions decrease with increasing field. This has been observed experimentally [7,58,59] by optical excitation, namely when the photogenerated carrier density increases, the oscillator strength increases, the spectral linewidth decreases and the QW transition energy shifts to higher energy.

CHAPTER 6

CONCLUSION AND FUTURE WORK

It is seen from this work that, it is more complicated to calculate the confinement energy levels for (111) quantum structures due to the built-in electric field. The effect of this field is to tilt the band edge of the well layer. As a result, the wave functions of the electrons and holes will be separated. A decrease of the overlap integral will reduce the oscillator strength and, therefore, lead to a decrease of the emission intensity, as compared to the same structure grown on a (001) substrate. Another effect is that the confined energy shifts to the bottom of the quantum well when the band edge is tilted.

We conclude that a larger energy shift is from a level with a smaller confined energy, which can be induced by a larger effective mass, a smaller well depth, or a wider well width. Another result we can observe from our work is a larger energy shift for a (111) quantum well than for a (001) well because of the larger heavy-hole effective masses in the (111) direction.

We have shown that the k-selection rule relaxed owing to a built-in field or strain-induced band structure modulation. This lowers the maximum gain of quantum well lasers for an injected carrier density compared to the flat band case.

The threshold characteristics of (111) oriented InGaAs / GaAs / AlGaAs quantum well lasers was compared with the equivalent (001) oriented devices by B. Gönül [57] and shown that the performance of (001) lasers better than that of (111) lasers. In those calculations parabolic approximation was used in the peak-gain versus carrier and current density. However, detailed investigation of valence band

structure including band mixing and coupling effects can provide us a more realistic subband structure which can significantly modify the valence band density of states. The realistic valence subband structure may bring some benefits for (111) oriented lasers compared to (001) lasers including reduced threshold carrier and current densities. A further investigation of a more accurate value of the magnitude of the piezoelectric field may significantly vary the effective field across the active layer at lasing threshold. The band-gap renormalization due to exchange and correlation is not considered in the previous work. However, it leads to a distinct lowering of the transition energies. In addition to the band-gap renormalization, the excition binding energy also lowers the transition energy which has not also been considered previously. In this thesis we gain a background and experience on these calculations and therefore a detailed investigation of combined effects of the realistic valence band structure, the accurate value of the strain-induced piezoelectric field, the variation of the effective field with carrier density, band-gap renormalization and exciton binding energy on the gain characteristics can be suggested as a future work.

REFERENCES

[1] E. Yablonovitch and E. O. Kane, J. Light Wave Technol., Vol. 6, (1992), pp. 1311-1315.

[2] T. Hayakawa, M. Kondo, T. Suyama, K. Takahashi, S. Yamamota and T. Hijikata, Jpn. J. Appl. Phys. 26, (1987), L302.

[3] T. Hayakawa, K. Takahashi, T. Suyama, M. Kondo, S. Yamamota and T. Hijikata, Jpn. J. Appl. Phys. 27, (1988), L300.

[4] H. Imamoto, F. Sato, K. Imanaka, and M. Shimura, Appl. Phys. Lett. 55, (1989), 115.

[5] J. W. Matthews, and A. E. Blakeslee, J. Cryst. Growth, 27, (1974), 118.

[6] D. L. Smith and C. Mailhot, Solid State Commun. 57, 919, 1986, Phys. Rev. Lett., 58, (1987), 1264.

[7] E. A. Caridi, T. Y. Chang, K. W. Goossen, and L. F. Eastman, Appl. Phys. Lett., 56, (1990) , 659.

[8] K. W. Goossen, E. A. Caridi, T. Y. Chang, J. B. Stark, D. A. B. Miller, and R. A. Morgan, Appl. Phys. Lett., 56, (1990), 715.

[9] I. Sela, D. E Watkins, B. K. Laurich, D. L. Smith, S. Subbanna, and H. Kroemer, Phys. Rev. B 43, (1991), 11884.

[10] H. Kroemer,A proposed class of heterojunction lasers, Proc. IEEE, 51, (1963) pp. 1782.

[11] Zh. I. Alferov, and R. F Kazarinov, Semiconductor laser with electrical pumping, U.S.S.R Patent 181737, (1963).

[12] J. M. Woodall, H. Rupprecht, and G. D Pettit, Solid State Device Conference, June 19, 1967, Santa Barbara, California.

[13] H. C. Casey, and M. B. Panish, Heterostructure lasers, (1968), Chapter 1, Academic Press, New York.

[14] Zh. Alferov, V. M. Andreev, D. Z. Zhilyaev, V. Yu, E. P. Morozov, E.L. Portnoi, and V. G. Sov. Phys. Semicond., 4, (1971), 1573.

[15] I. Hayashi, M. B. Panish, P. W. Poy, and S. Sumski, Appl.Phys. Lett.,17, (1970), 109.

[16] L. Esaki, and R. Tsu, IBM J. Res. Dev., 14, (1970), 61.

[17] R. Dingle, W. Wiegmann, and C. H. Henry, Phys. Rev. Lett., 33, (1974), 827.

[18] a) H. Okumura, S. Misawa, S. Yoshida, and S.Gonda, App. Phys. Lett.,46, (1985), 377.

b) S. R. Forrest, P. H. Schmidt, R. B. Wilson, M. L. Kaplan, Appl. Phys. Lett., 45, (1984), 1199.

[19] M. G. A. Bernard and B. Duraffourg, Phys. Stat. Sol., (1961), 699.

[20] L.W. Molenkamp, R. Eppenga, G. W. 'tHooft, P. Dawson, C.T. Foxon, and .J. Moore, Phys. Rev. B 38, (1988), 4314.

[21] T. Hayakawa, T. Suyama, K. Takahashi, M. Kondo, S. Yamamoto and T. Hijikata, Appl. Phys. Lett., 52, (1988), 399.

[22] A. Ghiti, W. Batty and E.P. O'Reilly, Superlattices and Microstructures, 7, (1990) 353.

[23] I. W. Tao, Electronics Lett., 28, (1992) 705.

[24] A. Ishihara and H. Watanabe, Jpn. J. Appl. Phys., 33, (1994), 1361.

[25] T. S. Moise, L.J. Guido, R. C. Barker, J. O. White, and A.R. Kost, Appl. Phys. Lett., 60, (1992), 2637.

[26] D. Sun and E. Towe, IEEE J. Quantum Electron., 30, (1994), 466.

[27] F. C. Frank, and J. H. Van der Merwe, Proc. Roy. Soc. (London), A198, 216.

[28] T. Anan, K. Nishi and S. Sugou, Appl. Phys. Lett., 60, (1992) 3159.

[29] P. Lawaetz, Phys. Rev. B, 4, (1971), 3460.

[30] R. People and S. K. Sputz, Phys. Rev. B, 41, (1990), 8431.

[31] G. Duggan, K. J. Moore, A. Raukema, G. Th. Jaarshma and K. Woodbridge, Phys. Rev. B, 45, (1992), 4494.

[32] G. C. Osbourn, J. Appl. Phys., 53, (1982), 1586.

[33] J. M. Hinckley and J. Singh, Phys. Rev. B, 42, (1990), 3546.

[34] G.E. Pikus and G.L. Bir, "Symmetry and Strain-induced Effects in Semiconductors", (1974), Chichester:Wiley.

[35] E.A. Caridi and J.B. Stark, Appl. Phys. Lett, 60, (1992), 1441.

[36] M.P.C.M. Krijn, G.W. t'Hooft, M.J.B. Boremans, P.J.A. Thijs, J.J.M. Binsma, L.F. Tiemeijer, and C.J. van der Poel, Appl. Phys. Lett., 61, (1992), 1772.

[37] T. S. Moise, L. J. Guido, and R. C. Barker, J. Appl. Phys.,74, (1993), 4681.

[38] T. A. Fisher, R. A. Hogg, A. K. Willcox, D. M. Whittaker, M. S. Skolnick, D. J. Mowbray, J. P. R. David, A. S. Pabla, G. J. Rees, R. Grey, J. L. Sanchez - Rojas, J. Woodhead, G. Hill, M. A. Pate and P. N. Robson, Solid - St. Electronics, 37, (1994) 645.

[39] J.L. Sanchez-Rojas, A. Sacedon, F. Gonzalez-Sanz, E. Calleja, and E. Munoz, Appl. Phys. Lett., 65, (1994), 2042.

[40] G. Bastard and J. A. Brum, IEEE J. Quantum Electron.QE-22, (1986), 1625.

[41] W. T. Tsang, Appl. Phys. Lett., Vol. 39, (1981), pp. 786-788.

[42] Y. Arakawa, K. Vahala and A. Yariv, App. Phys. Lett., vol. 45, (1984), pp. 950-952.

[43] M. Asada, A. Kameyama, and Y. Suematsu, IEEE J. Quantum Electron., vol. QE-20, (1984), pp. 745.

[44] Y. Arakawa, and A. Yariv, Iqwe IEEE J. Quantum Electron., vol. 21, (1985), pp. 1666-1674.

[45] W. T. Tsang, Appl. Phys. Lett., 39 (1981), 768.

[46] D. Kasemmet, C. S. Hong, N. B. Patel and P. D. Dapkus, IEEE J. Quantum Electron. QE-19, (1983), 1025.

[47] S. Colak, R. Eppenga and M. F. Shuurmans, IEEE J. Quantum Electron. QE-23, (1987), 960.

[48] J. P. Leburton and K. Hess, J. Vac. Sci. Technol., B1, (1983), 415.

[49] M. Yamanishi and I. Suemune, Japan. J. Appl. Phys., 23, (1984), L35.

[50] G. Jones, Ph. D Thesis, "Effects of Elastic Strain on the Performance of Semiconductor Lasers", University of Surrey, (1994).

[51] M. Yamada and Y. Suematsu, J. Appl. Phys., 52, (1981), 2653.

[52] M. Yamada, H. Ishiguro and H. Hagato, Japan. J. Appl. Phys., 19, (1980), 135.

[53] M. Takehima, Phys. Rev. B, 36, (1987), 8082.

[54] M. Asada, Y. Yasuyuki and Y. Suematsu, IEEE J. Quantum Electron., QE-22, (1986), 1915.

[55] M. Asada and Y. Suematsu, IEEE J. Quantum Electron. QE-21, (1985), 434.

[56] P.S. Zory, "Quantum-Well Lasers", Academic Press, US, (1993).

[57] B. Gönül, Ph. D Thesis, "A Theoretical Study of the Threshold Current of Quantum Well Lasers", University of Surrey, (1995).

[58] T.S. Moise, J.C. Beggy, T.J. Cunningham, S. Seshadri, and R.C. Barker, J. Electron. Mater., 21, (1992), 119.

[59] D.A. B. Miller, D.S. Chemla, T.C. Damen, A.C. Gossard, W. Weigmann, T.H. Wood, and C.A. Burrus, Phys. Rev. B, 32 (1985) 1043.

APPENDIX A

A.1. Material Parameters

The linear interpolation scheme is known to be a useful tool for estimating some physical parameters of alloy compounds. Of particular interest is the deviation of material parameters from linearity with respect to the alloy composition. The material parameters for the device from well and barrier compositions are the well-barrier-width and growth orientations. If one uses scheme, the ternary material parameter (T) can be derived from binary parameters (B's) by

$$\begin{aligned} T_{ABC}(x) &= xB_{AB} + (1-x)B_{AC} \\ &\equiv a + bx \end{aligned} \tag{A.1}$$

for alloys of the form AB_xC_{1-x}, where $a = B_{AC}$ and $b = (B_{AB} - B_{AC})$. Some experimental data, however, deviate from linearity relation of Eqn.(A.1), and have an approximately quadratic dependence on the mole fraction of one compound x,

$$T_{ABC}(x) = a + bx + cx^2, \tag{A.2}$$

where c is referred to as a nonlinear or bowing parameter. The parameter a and b are determined by the values observed in the pure binary compounds. The material such as the lattice constants vary linearly with composition x, and therefore, Eqn.(A.1) gives a good estimate for the relevant alloy-compound parameters.

The quaternary alloy $A_xB_{1-x}C_yD_{1-y}$ are binary compound values, say B_{AC}, B_{AD}, B_{BC} and B_{BD} and the quaternary material parameters (Q) interpolated from the following expressions,

$$Q_{ABCD}(x,y) = \frac{x(1-x)[(1-y)T_{ABD} + yT_{ABC}]}{x(1-x)+y(1-y)} + \frac{y(1-y)[(1-x)T_{ACD} + yT_{BCD}]}{x(1-x)+y(1-y)}, \qquad (A.3)$$

where

$$T_{ABC}(x) = x\, B_{AC} + (1-x)\, B_{BC} + C_{ABC}\, x\,(1-x). \qquad (A.4)$$

C_{ABC} is the ternary bowing parameter, x is the fractional composition of A in $A_x B_{1-x} C$, and y is the fractional composition of C in $A_x B_{1-x} C_y D_{1-y}$.

The lattice constant for any given composition of binary, ternary and quaternary well material is compered with that of substrate material to determine whether the structure under investigation is an unstrained or strained laser device. Lattice mismatch has two important effects on the electronic band structure of the semiconductor, for (001) oriented laser structure. Moreover, the effect of strain on the band structure varies with growth orientation.

The advantages are traceable to the control which heterostructures provide over the motion of charge carriers. (In optoelectronic devices, the ability to confine the optical radiation is also extremely important.) This control can be exerted in the form of selective energy barriers (barriers for one carrier type different from that for the other) or quantum-scale potential variations.